Modeling the drying process in hard carbon electrodes based on the phase-field method

M. Weichel[1,2,*] M. Reder[2,3] S. Daubner[1,2] J. Klemens,[4] D. Burger[4] P. Scharfer[4] W. Schabel[4] B. Nestler,[1,2,3,†] and D. Schneider[1,2,3]

[1]*Institute of Nanotechnology (INT), Karlsruhe Institute of Technology, Hermann-von-Helmholtz-Platz 1, 76344 Eggenstein-Leopoldshafen, Germany*

[2]*Institute for Applied Materials (IAM-MMS), Karlsruhe Institute of Technology, Strasse am Forum 7, 76131 Karlsruhe, Germany*

[3]*Institute of Digital Materials Science (IDM), Karlsruhe University of Applied Sciences, Moltkestrasse 30, 76133 Karlsruhe, Germany*

[4]*Thin Film Technology (TFT), Karlsruhe Institute of Technology (KIT), Strasse am Forum 7, 76131 Karlsruhe, Germany*

(Received 15 November 2024; revised 27 January 2025; accepted 26 February 2025; published 26 March 2025)

The present work addresses the simulation of pore emptying during the drying of battery electrodes. For this purpose, a model based on the multiphase-field (MPF) method is used, since it is an established approach for modeling and simulating multiphysical problems. A model based on phase fields is introduced that takes into account fluid flow, capillary effects, and wetting behavior, all of which play an important role in drying. In addition, the MPF method makes it possible to track the movement of the liquid-air interface without computationally expensive adaptive mesh generation. The presented model is used to investigate pore emptying in real hard carbon microstructures. For this purpose, the microstructures of real dried electrodes are used as input for the simulations. The simulations performed here demonstrate the importance of considering the resolved microstructural information compared to models that rely only on statistical geometry parameters such as pore size distributions. The influence of various parameters such as different microstructures, fluid viscosity, and the contact angle on pore emptying are investigated. In addition, this work establishes a correlation between the capillary number and the breakthrough time of the solvent as well as the height difference of the solvent front at the time of breakthrough. The results indicate that the drying process can be optimized by doping the particle surface, which changes the contact angle between the fluids and the particles.

DOI: 10.1103/PhysRevMaterials.9.035403

I. INTRODUCTION

The demand for energy storage systems is rising, leading to an increased production of lithium-ion batteries, but postlithium alternatives such as sodium-ion batteries (SIBs) are also entering the market [1,2]. SIBs are a drop-in technology, in the sense that established production processes can be adapted from lithium-ion batteries [3], potentially saving costs and time for upscaling. However, even with the most modern production processes, there is still potential for a further reduction in energy consumption, which has an impact on costs and sustainability, as drying the battery electrodes in particular is energy intensive [4]. In general, the production of battery electrodes can be divided into five steps: slurry mixing, coating, drying, calendering, and cutting. The slurry consists of active material particles, binding agents, conductive additives, and a solvent. After the slurry is coated onto a substrate, the porous electrode microstructure is formed as a result of the evaporation of the solvent during the drying process. The resulting microstructure affects the electrochemical and mechanical properties of the final battery. The microstructure formation can be divided into two stages. During the first stage, evaporation of the solvent causes the film height to shrink, resulting in a porous structure, while in the second stage, this porous microstructure is emptied by evaporation. The distribution of the binder in the microstructure is particularly important for the resulting electrochemical and mechanical properties. It depends on the drying rate, the pore size distribution, and other properties of the slurry. If the drying rate is too high, a migration of binder away from the substrate is observed, which leads to a reduced adhesive strength between the electrode and the substrate. In addition, the accumulation of binder on the electrode surface can lead to pore clogging, which has a negative impact on electrochemical key performance indicators such as rate capability [5–16]. A detailed understanding of the process-property relationship of drying and the binder distribution offers great potential for battery optimization.

Modeling and simulation can provide important insights into the drying process by predicting the resulting properties from multiple process parameters. The existing modeling approaches for battery production can be divided into homogenized continuum models [17,18], models based on coarse-grained molecular dynamics [19,20], models based on the discrete element method [21], and spatially resolved continuum models [22,23].

Homogenized continuum approaches are based on simplified mathematical equations to investigate the influence of

*Contact author: marcel.weichel@kit.edu
†Contact author: britta.nestler@kit.edu

process parameters on drying. Spatial dimensions are often reduced and the flow is calculated according to Darcy's law [24], instead of the Navier-Stokes equations. Such approaches are less computationally intensive, but at the same time limited due to the underlying assumptions. Investigation of different drying rates has been carried out by Stein *et al.* [25]. By analyzing the spatial distribution of the additives, they show that a slow two-stage drying process is superior to a fast one-stage drying process. Another mathematical model is introduced by Susarla *et al.* [24], which is based on volume averaging and the reduction to one dimension, taking into account additional effects of mass and heat transport as well as phase change. By using multizone drying, they show that the energy required for drying can be reduced by 50%. The additives are not taken into account in their simulations. The work by Font *et al.* [17] shows that the binder distribution is more homogeneous at a low drying rate. The approach of a diffusion-convection equation for the binder is investigated by Zhirul *et al.* [18]. Both approaches agree with the trends from experimental observations but lack the modeling of capillary transport phenomena, which are the main cause of binder migration. Models based on coarse-grained molecular dynamics are often based on the idea of combining the carbon black (CB) and the binder in the CB binder domain (CBD). The evaporation is then modeled by the shrinkage of these CBD particles, since the solvent is contained in them, while the movement of the solvent is implicitly described by Brownian motion. They are therefore not suitable for simulating the process of pore emptying, which is the subject of this paper. The interactions between the different particles are calculated with coarse-grained molecular dynamics and fitted by a Lennard-Jones potential with shifted force and a granular Hertzian potential. Forouzan *et al.* [19] describe the simulation of the manufacturing process of lithium-ion cathodes with such an approach on the mesoscale. They investigate numerous physical parameters such as viscosity, shrinkage ratio, and the volume fractions of the phases and compare the results with data from experiments to validate their model. Another work that uses such a modeling approach for the drying step can be found in the ARTISTIC project. It is based on the work of Forouzan *et al.* [19] and makes it possible to simulate various production steps of the electrode production and electrochemical experiments [20,26–34]. In addition, this model enables the simulation of nonspherical particles [35]. Discrete element methods are suitable for describing the particle movement during the first stage of microstructure formation during drying (film shrinkage) and thus simulating the resulting microstructure. In the work by Lippke *et al.* [21], this method is used to calculate the microstructure formation. In an extension of this work, the discrete element method is extended with further models so that, in addition to film shrinkage, drying kinetics, binder distribution, and calendering can also be simulated [36]. Since discrete element methods use surrogate models for fluid effects, they cannot resolve the drying front and do not take into account the dynamics of the contact lines and thus the effects of surface wettability. They are therefore not suitable for treating the pore emptying process, which is assumed to have the greatest influence on binder migration.

A spatially resolved continuum approach is applied by Wolf *et al.* [22]. They model the structural formation during the drying of the battery electrodes. For this purpose, they combine the discrete element method to describe the particle movement and the volume-of-fluid method [37] to distinguish the fluid phases. Scaling is used to keep the simulation time short. However, some physical features that are important for the drying of electrodes are not considered. These are, for example, the wetting behavior including the contact angle, which is important for pore emptying. Additionally, their approach is limited to spherical particles and cannot address the microstructure of nonspherical particles, such as those found in hard carbon electrodes. The pore emptying that occurs during the drying of battery electrodes has not been explicitly investigated using the models described above. Models that can take pore emptying into account can be divided into two different groups [38]. On the one hand, there are the discrete pore network models (PNMs), and on the other hand, continuum models (CMs) [39]. The two model approaches differ in their length scale. PNMs work on the scale of pores, while continuum models work on the macroscopic length scale. PNMs were first introduced by Prat *et al.* [40] and have been continuously developed since then. For example, they have been used to investigate the influence of properties such as the pore structure and viscosity [41–44]. PNMs are surrogate models and therefore cannot depict spatially resolved microstructures directly. The information about the microstructures is considered via statistical variables in PNMs. Furthermore, the computational costs grow if the overall resolution of the simulation scale is increased [38]. The network representation can be improved using image-based PNMs, which employ real pore-scale spatial correlations from microstructure images [45]. One advantage of homogenized continuum models is their capacity to simulate large-scale areas. However, the influence of the microstructure is not taken into account directly, as it enters the models via effective parameters. When simulating the drying of battery electrodes within the framework of spatially resolved continuum mechanics, several effects must be taken into account, namely, the two-phase flow including capillary effects, the movement of the liquid-air interface, and the wetting behavior within complex electrode microstructures. Most models based on homogenized continuum approaches, coarse-grained molecular dynamics, or the discrete element method do not consider these effects. Extensions to incorporate wettability effects in such models can be found, for example, in [46,47]. However, they do not directly track the interfaces on the pore scale but model wettability effects based on a potential using geometrical assumptions, e.g., the pores having the cross section of a duct [46]. The multiphase-field (MPF) method offers great potential to address these challenges, as it intrinsically covers multiple phases [48,49], the parametrization of complex microstructures [50,51], and the evolution of interfaces. Furthermore, coupling with fluid flow has been used in various works [52–54], including the simulation of rigid-body motion in a fluid [53] and two-phase flows with immersed rigid bodies [54]. The MPF approach is also well established in the context of phase transitions and chemical couplings in battery systems [55,56], which simplifies future extensions in terms of model development and multiscale modeling.

In the present work, a model is formulated, validated, and subsequently applied to microstructures of hard carbon

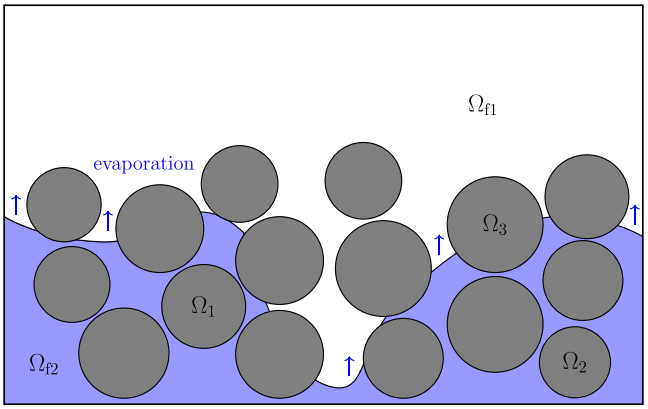

FIG. 1. Schematic representation of the drying process of the battery electrodes.

electrodes obtained from scanning electron microscopy (SEM) data. The phase-field framework is based on the work of Reder *et al.* [54], but includes significant extensions to additionally account for the evaporation of solvent. In Sec. II, the model formulation is presented in detail. Before we investigate the drying of two hard carbon anode structures for sodium-ion batteries in Sec. IV, the model is validated based on three example cases (see Sec. III). Together with experimental material parameters, the SEM images are used as an input to study the influence of the drying parameters on the resulting pore emptying behavior. This approach provides insights into the spatial velocity field within these complex microstructures, which is related to the binder transport and, thus, the final binder distribution. The influence of viscosity, pore size distribution, and the wetting angle between fluid and solid is studied, as these parameters may influence the binder migration. A summary and a discussion of future work can be found in Sec. V.

II. MATHEMATICAL FORMULATION

Problem specification. Figure 1 shows a schematic representation of the problem addressed in this work. A multiphase problem is considered, which generally consists of $N^{\mathrm{f}} = 2$ different fluid phases and N^{s} different solid phases. The computational domain $\Omega = \Omega_{\mathrm{f}} \cup \Omega_{\mathrm{s}}$ is the union of the domains Ω_{f} and Ω_{s}, which are occupied by fluid and solid phases, respectively. Both the fluid and solid domains can be decomposed into the domain of the individual fluid and solid phases, so that $\Omega_{\mathrm{f}} = \Omega_{\mathrm{f1}} \cup \Omega_{\mathrm{f2}}$ and $\Omega_{\mathrm{s}} = \cup_{p=1}^{N^{\mathrm{s}}} \Omega_p$ hold. The model in the present work is based on the approach by Reder *et al.* [54], which is adjusted and extended to mimic a phase transformation in the context of battery electrode drying. First, a model for the two-phase flow assuming $\Omega_{\mathrm{s}} = \emptyset$ is derived, which is based on the approach of Hohenberg *et al.* [57] (model H) and is extended by a term that accounts for the phase transformation in order to mimic evaporation. This model is then adapted to a diffuse-domain formulation to include solid phases ($\Omega_{\mathrm{s}} \neq \emptyset$). Therefore, the boundary conditions at the fluid-solid interface are included diffusely, based on the procedure of Li *et al.* [58].

Two-phase flow. Regarding the fluid dynamics, the Navier-Stokes equation is considered, taking the form

$$\rho \frac{\partial \boldsymbol{u}}{\partial t} + \rho \nabla \boldsymbol{u} \cdot \boldsymbol{u} = -\nabla p + \nabla \cdot [\mu(\nabla \boldsymbol{u} + (\nabla \boldsymbol{u})^{\mathrm{T}})] + \boldsymbol{K} + \rho \boldsymbol{f}_{\mathrm{V}}, \tag{1a}$$

$$\nabla \cdot \boldsymbol{u} = 0. \tag{1b}$$

Thereby, from Eqs. (1a) and (1b), the momentum and continuity equations for incompressible flow can be identified. The velocity field is represented by $\boldsymbol{u}$, the mass density by ρ, the pressure by p, the dynamic viscosity by μ, and the body forces by $\boldsymbol{f}_{\mathrm{V}}$. The capillary term is denoted as $\boldsymbol{K}$ and will be specified later. In general, the dynamic viscosity μ can depend on the temperature and, in the context of generalized Newtonian fluids, on the shear rate (cf., e.g., [59]). The geometry parametrization is achieved using a phase-field method. In contrast to a sharp theory, the dividing surfaces between different fluids are replaced by a diffuse transition region, also called diffuse interface (cf. [60] for a detailed discussion). Therefore, phase variables $\varphi_\alpha(\boldsymbol{x}, t) \in [0, 1]$ are introduced for each of the N considered phases. These can be considered as the local volume fraction of a phase α at a specific spatial point $\boldsymbol{x}$ and time t. It follows that the capillary term $\boldsymbol{K} = \boldsymbol{K}(\varphi_1, \varphi_2, \ldots, \varphi_N)$ and the physical parameters $\rho = \rho(\varphi_1, \varphi_2, \ldots, \varphi_N)$ and $\mu = \mu(\varphi_1, \varphi_2, \ldots, \varphi_N)$ depend on the phase variables.

For two-phase flow, it is sufficient to consider one phase variable, and so the field $\tilde{\varphi} := \varphi_1$ is introduced. An Allen-Cahn approach or a Cahn-Hilliard approach can be used to describe the temporal evolution of the phase variables. Details and a comparison can be found in [61]. Due to numerical considerations, the Allen-Cahn approach is employed in the present work. It yields

$$\dot{\tilde{\varphi}} = \partial_t \tilde{\varphi} + \nabla \tilde{\varphi} \cdot \boldsymbol{u} = M(\beta \partial_{\tilde{\varphi}} \psi - \alpha \nabla^2 \tilde{\varphi}), \quad \boldsymbol{x} \in \Omega_{\mathrm{f}}, \tag{2}$$

with the mobility M and the free energy potential $\psi(\tilde{\varphi})$. Here, the partial derivative operator with respect to $(\cdot)$ is abbreviated as $\partial_{(\cdot)} := \partial / \partial(\cdot)$. The free energy potential can be selected in various ways. In our case, we use a well potential given by $\psi(\tilde{\varphi}) = \tilde{\varphi}^2(1 - \tilde{\varphi})^2$. The coefficients α and β are chosen as $\alpha = \sigma\varepsilon$ and $\beta = 18\frac{\sigma}{\varepsilon}$, where σ is the surface energy density and ε scales the diffuse interface width. The value $\varepsilon = 5\Delta x$ is used in this work. Moreover, the evolution equation can be written as

$$\dot{\tilde{\varphi}} = M\left[\frac{36\sigma}{\varepsilon}(2\tilde{\varphi}^3 - 3\tilde{\varphi}^2 + \tilde{\varphi}) - \sigma\varepsilon\nabla^2\tilde{\varphi}\right], \quad \boldsymbol{x} \in \Omega_{\mathrm{f}}. \tag{3}$$

Additionally the wetting boundary condition

$$\alpha \nabla \tilde{\varphi} \cdot \boldsymbol{n}^{\mathrm{fs}} = (\sigma_{2\mathrm{s}} - \sigma_{1\mathrm{s}}) \partial_{\tilde{\varphi}} h^{\mathrm{ff}}(\tilde{\varphi}), \quad \boldsymbol{x} \in \partial\Omega_{\mathrm{f}}, \tag{4}$$

is considered, where $\boldsymbol{n}^{\mathrm{fs}}$ is the outward-pointing normal vector on the boundary of Ω_{f}. Furthermore, $\sigma_{2\mathrm{s}}$ and $\sigma_{1\mathrm{s}}$ are surface energies between the solid and the respective fluid phase, while h^{ff} is an interpolation function for the two fluids, which will be specified later. Using the surface energies between the different phases, the contact can be described by means of Young's law as

$$\cos(\theta) = \frac{\sigma_{2\mathrm{s}} - \sigma_{1\mathrm{s}}}{\sigma} \tag{5}$$

as the contact angle regarding fluid 1, while $\Theta = 180^\circ - \theta$ in this work is referred to as the contact angle regarding fluid 2.

Capillarity term. The capillarity term $\boldsymbol{K}$ in Navier-Stokes equation (1) accounts for the curvature minimization due to the surface tension between different fluids. There are various ways to model the capillarity term [62]. In this work, we take advantage of the so-called potential form

$$\boldsymbol{K}(\tilde{\varphi}) = -\tilde{\varphi}\nabla\Phi, \tag{6}$$

where $\Phi = \beta\partial_{\tilde{\varphi}}\psi - \alpha\nabla^2\tilde{\varphi}$. For a further discussion, see Jacqmin *et al.* [63]. The Allen-Cahn approach from Eq. (3) intrinsically exhibits curvature-minimizing dynamics. This leads to undesirable dynamics, as surface tension effects are already covered by the capillary term, which provides a corresponding velocity contribution. The additional surface-minimizing dynamics in the Allen-Cahn equation can be removed [64], which is achieved by the approach of Sun *et al.* [65]. It follows for the phase field equation

$$\dot{\tilde{\varphi}} = M\left[\frac{36\sigma}{\varepsilon}(2\tilde{\varphi}^3 - 3\tilde{\varphi}^2 + \tilde{\varphi}) - \sigma\varepsilon(\nabla^2\tilde{\varphi} - ||\nabla\tilde{\varphi}||\nabla\cdot\boldsymbol{n})\right], \quad \boldsymbol{x}\in\Omega_\mathrm{f}, \tag{7}$$

with $\boldsymbol{n} = \frac{\nabla\tilde{\varphi}}{||\nabla\tilde{\varphi}||}$. This extension ensures that the influence of surface tension is not overestimated.

Evaporation term. The present model is intended to mimic the drying process in battery electrode systems. The evaporation phenomenon can be modeled by a phase transformation. For this purpose, we insert a term $v^\mathrm{e}||\nabla\tilde{\varphi}||$ into Eq. (7) to model the motion of the interface with a phase transformation velocity v^e and a term $||\nabla\tilde{\varphi}||$ that distributes the velocity over the diffuse interface. Thus, Eq. (7) is modified as follows:

$$\dot{\tilde{\varphi}} = M\left[\frac{36\sigma}{\varepsilon}(2\tilde{\varphi}^3 - 3\tilde{\varphi}^2 + \tilde{\varphi}) - \sigma\varepsilon(\nabla^2\tilde{\varphi} - ||\nabla\tilde{\varphi}||\nabla\cdot\boldsymbol{n})\right] + v^\mathrm{e}||\nabla\tilde{\varphi}||, \quad \boldsymbol{x}\in\Omega_\mathrm{f}. \tag{8}$$

According to Eq. (E5), the velocity v^e is directly related to the evaporation rate (mass flux per area in $\mathrm{kg\,m^{-2}\,s^{-1}}$), by means of the factor κ (unit $\mathrm{s^{-1}}$). It should be noted that a constant evaporation rate occurs for most of the pore emptying [6], which means that κ is constant over time. By incorporating κ, we can calculate the theoretical total volume fraction of the solvent,

$$\chi^{t_n}_{\mathrm{solvent,theo}} = -\kappa t_n + \chi^0_\mathrm{solvent}, \tag{9}$$

where t_n is the time and χ^0_solvent denotes the initial volume fraction of the fluid that evaporates. The derivation of Eq. (9) can be found in Appendix E. The velocity v^e then results in

$$v^\mathrm{e} = -\frac{\chi^{t_n}_{\mathrm{solvent,theo}} - \chi^{t_n}_\mathrm{film}}{\int||\nabla\tilde{\varphi}||\mathrm{d}V\,\Delta t}V^0_\mathrm{film}, \tag{10}$$

where V^0_film is the total film volume at $t = 0$. The term of the driving force can be interpreted as a Lagrange multiplier, which ensures the target volume fraction $\chi^{t_n}_{\mathrm{solvent,theo}}$. For the special case $\kappa = 0$, the Allen-Cahn equation is volume preserving (see Appendix B). Furthermore, the presented model includes evaporation as an effective rate which is evenly distributed along the fluid-fluid interface; i.e., the mass transfer in the gas phase by vapor diffusion is not explicitly modeled.

Multiphase flow with rigid-body coupling. To apply the model-H approach [57] to the two-phase flow with solid phases, which exhibit a diffuse solid interface, a normalization approach according to Reder *et al.* [54] is employed. This normalization splits the problem into two subproblems. First, we introduce the local volume fraction of all fluid and solid phases in the form of

$$\varphi^\mathrm{f} = \frac{V^\mathrm{f}}{V} = \sum_{\alpha=1}^{N^\mathrm{f}}\varphi^\mathrm{f}_\alpha \quad\text{and}\quad \varphi^\mathrm{s} = \frac{V^\mathrm{s}}{V} = \sum_{\alpha=1}^{N^\mathrm{s}}\varphi^\mathrm{s}_\alpha, \tag{11}$$

with V^f as the total fluid and V^s as the total solid volume in a representative volume element V. Moreover, the normalization for the fluid phases is done by

$$\tilde{\varphi}^\mathrm{f}_\alpha := \frac{\varphi^\mathrm{f}_\alpha}{\varphi^\mathrm{f}}, \quad \text{for} \quad \varphi^\mathrm{f} > 0, \tag{12}$$

where $\tilde{\varphi} := \tilde{\varphi}_1$, in the case of two fluids, including the sum condition $\sum_{\alpha=1}^{N^\mathrm{f}}\tilde{\varphi}^\mathrm{f}_\alpha = 1$. Regarding the normalized phase variable $\tilde{\varphi}$, the evolution equation (8) can be employed. For the entire set of partial differential equations (PDEs), the appropriate boundary conditions at the fluid-solid interface must be defined via the diffuse interface. In general, the approach of Li *et al.* [58] can be used to formulate boundary conditions for a diffuse interface between different phases. The boundary conditions can be of the Robin, Dirichlet, or Neumann type. With regard to Navier-Stokes equation system (1), we follow the approach of Beckermann *et al.* [66] for the diffusive application of the no-slip boundary condition. As for the wetting boundary condition (4), the general approach is used, e.g., in [54,67], to derive diffuse wetting boundary conditions in a Cahn-Hilliard formulation. The derivation of the corresponding Allen-Cahn formulation can be found in Appendix D. Thus, the set of PDEs for the whole domain $\boldsymbol{x}\in\Omega$ that need to be solved is as follows:

$$\partial_t(\rho h^\mathrm{fs}\boldsymbol{u}) = -\nabla\cdot(\rho h^\mathrm{fs}\boldsymbol{u}\otimes\boldsymbol{u}) - h^\mathrm{fs}\nabla p + \nabla\cdot(h^\mathrm{fs}\mu\nabla\boldsymbol{u}) + \boldsymbol{u}\nabla\cdot(\mu\nabla h^\mathrm{fs}) + \rho h^\mathrm{fs}\boldsymbol{f}_\mathrm{V} + h^\mathrm{fs}\boldsymbol{K}, \tag{13a}$$

$$0 = \nabla\cdot(h^\mathrm{fs}\boldsymbol{u}), \tag{13b}$$

$$h^\mathrm{fs}\dot{\tilde{\varphi}} = M\Big[\beta h^\mathrm{fs}\partial_{\tilde{\varphi}}\psi - \alpha\Big(\nabla\cdot h^\mathrm{fs}\nabla\tilde{\varphi} - h^\mathrm{fs}||\nabla\tilde{\varphi}||\nabla\cdot\frac{\nabla\tilde{\varphi}}{||\nabla\tilde{\varphi}||}\Big) - \partial_{\varphi^\mathrm{f}}h^\mathrm{fs}||\nabla\varphi^\mathrm{f}||(\sigma_{2\mathrm{s}} - \sigma_{1\mathrm{s}})\partial_{\tilde{\varphi}}h^\mathrm{ff}\Big] + h^\mathrm{fs}v^\mathrm{e}||\nabla\tilde{\varphi}||. \tag{13c}$$

The interpolation functions $h^\mathrm{fs}(\varphi^\mathrm{f}) = (\varphi^\mathrm{f})^2(3 - 2\varphi^\mathrm{f})$ and $h^\mathrm{ff}(\tilde{\varphi}) = \tilde{\varphi}^2(3 - 2\tilde{\varphi})$ for the fluid-solid and fluid-fluid interface are employed. For the phase variable of the fluid, a sinus profile of the form $\varphi^\mathrm{f}(\eta) = 1/2[1 - \sin(\pi\eta/\delta_\mathrm{fs})]$ is applied, with δ_fs denoting the interface width and η the normal coordinate pointing from the fluid to the solid at the fluid-solid interface.

Numerical treatment. This section briefly describes the algorithm for phase-field equation (13c). The approach of [53,54] is used to solve the Navier-Stokes equation. A

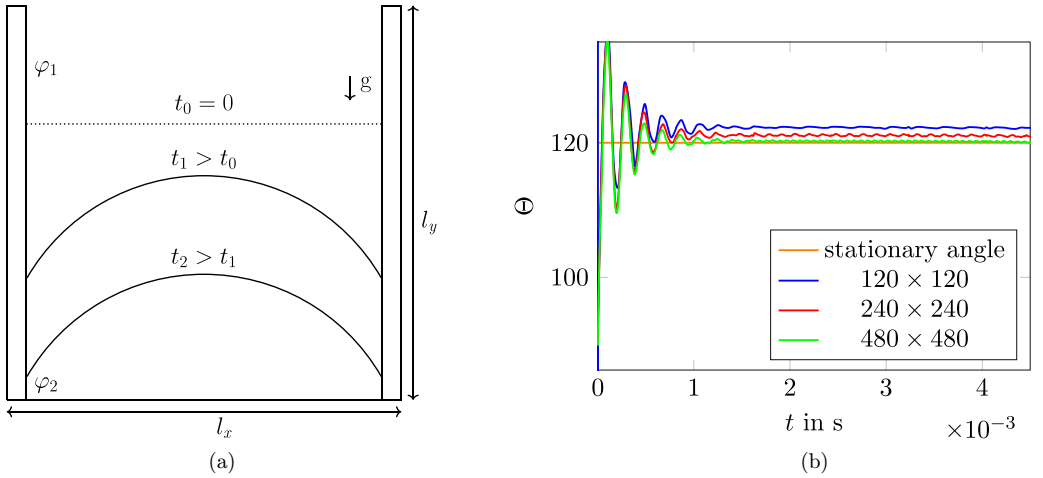

FIG. 2. Validation case of an evaporating fluid in a capillary. (a) Schematic representation of the moving contact line problem. (b) Contact angle as a function of time for different grid refinements.

fractional step method is used for the phase-field equation, which is represented as follows:

(1) First, we solve only the convective term, which gives

$$(\tilde{\varphi}^*) = \int_{t_n}^{t_{n+1}} -\nabla\tilde{\varphi}^n \cdot \boldsymbol{u}\ \mathrm{d}t. \tag{14}$$

(2) We then introduce the pseudotime t^* and then calculate the equilibrium according to

$$\frac{\partial\tilde{\varphi}^{**}}{\partial t^*} = M\Bigg[\frac{36\sigma}{\varepsilon}(2\tilde{\varphi}^{*3} - 3\tilde{\varphi}^{*2} + \tilde{\varphi}^*) - \frac{\sigma\varepsilon}{h^{\mathrm{fs}}}\left(\nabla\cdot h^{\mathrm{fs}}\nabla\tilde{\varphi}^* - h^{\mathrm{fs}}||\nabla\tilde{\varphi}^*||\nabla\cdot\frac{\nabla\tilde{\varphi}^*}{||\nabla\tilde{\varphi}^*||}\right) - \frac{\partial_{\varphi^*}h^{\mathrm{fs}}(\varphi^*)||\nabla\varphi^*||}{h^{\mathrm{fs}}}(\sigma_{2\mathrm{s}} - \sigma_{1\mathrm{s}})\partial_{\tilde{\varphi}}h^{\mathrm{ff}}(\tilde{\varphi}^*)\Bigg]. \tag{15}$$

(3) In the last step, we apply the evaporation term,

$$\tilde{\varphi}^{n+1} = \tilde{\varphi}^{**} + \int_{t_n}^{t_{n+1}} v^e||\nabla\tilde{\varphi}^{**}||\ \mathrm{d}t. \tag{16}$$

By splitting the phase-field equation, a more accurate representation of the equilibrium profile at the interface and the evaporation rate is achieved. The implementation was done using an in-house solver (PACD3D) [68], which employs parallelization via message-passing interface (MPI). Herein, the discretization of the PDEs is achieved by employing the finite difference method on a Cartesian grid. An explicit Euler method is used for time integration. To discretize the convective term in the phase-field equation, we employed the second-order-accurate OSPRE flux limiter scheme [69]. The Navier-Stokes solution is obtained by a Chorin-type projection method on a staggered grid arrangement for the velocity (cf. Sec. 2.6 of [53] for more details). Regarding the spatial discretization schemes employed for the Navier-Stokes equation, we refer to Sec. 3.3 of [54], where similar schemes are used. Additionally, a dynamic adjustment of the time step according to a Courant-Friedrichs-Lewy condition is conducted to ensure numerical stability for all PDEs following the condition of non-negative coefficients according to [70]. All simulations are conducted on a 64-core system equipped with AMD EPYC™ 7452 processors.

III. VALIDATION

The following section is divided into three main sections to discuss the validation of the model. Section III A examines the contact angle that occurs at a moving contact line between three phases. Furthermore, in Sec. III B, the rise height of a liquid in a capillary is calculated and compared with the analytical solution, while in the final section (Sec. III C), the influence of different pore sizes on the drying process is investigated.

A. Contact angle at a moving contact line

Setup and parameters. Figure 2(a) depicts the schematic representation of the first validation case. The physical dimensions are $l_{\mathrm{x}} = 56.0\,\mu\mathrm{m}$ and $l_{\mathrm{y}} = 56.0\,\mu\mathrm{m}$, with l_{x} as the characteristic length l_{char}. A value of $\sigma = 7.3 \times 10^{-2}\ \mathrm{N\,m^{-1}}$ is set for the surface tension and a macroscopic equilibrium contact angle of $\theta = 60^\circ$ is employed. Furthermore, the gravitational body force is given by $g = 9.81\ \mathrm{m\,s^{-2}}$, whereas for the fluids the following physical parameters apply. Fluid 1 φ_1 has a density of $\rho_1 = 1.225\ \mathrm{kg\,m^{-3}}$ and a viscosity of $\mu_1 = 1.72 \times 10^{-5}\ \mathrm{Pa\,s}$, while fluid 2 φ_2 is defined by a density of $\rho_2 = 997.0\ \mathrm{kg\,m^{-3}}$ and a viscosity of $\mu_2 = 1.0 \times 10^{-3}\ \mathrm{Pa\,s}$. In addition, the factor κ equals $100\ \mathrm{s^{-1}}$ and the mobility is set to $M = 30.0\ \mathrm{m\,s\,kg^{-1}}$.

Results. Fig. 2(b) shows the macroscopic contact angle $\Theta = 180^\circ - \theta$, which is calculated according to the method given in Appendix C, as a function of the time in seconds, for different grid refinements. The initially flat fluid interface becomes curved as the contact angle is established at the contact line where the solid and both fluid phases meet. Oscillating movements of the interface are observed due to inertia effects, whereby the oscillations are damped over time. After some time, the calculated contact angle settles to an average value Θ_{mean}, which shows only small fluctuations. The mean contact angles 121.95°, 120.85°, and 120.12° are

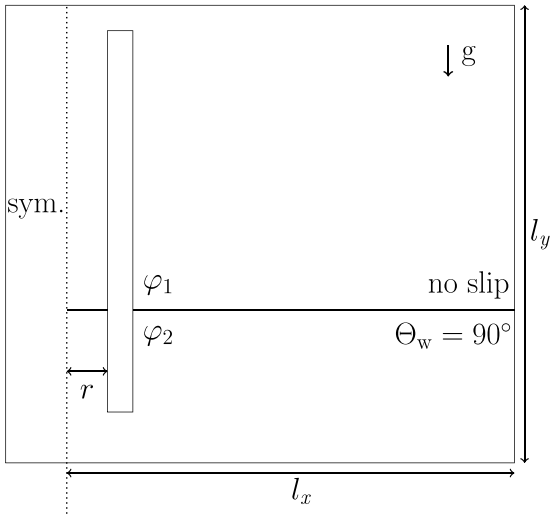

FIG. 3. Initial setup for the rise of a fluid in a capillary.

computationally measured for the resolutions 120×120, 240×240, and 480×480. It can be seen that the mean contact angle approaches the equilibrium angle with increasing resolution. Additionally, the oscillation amplitude of Θ decreases with the refinement. It should be noted that the local contact angle is applied immediately according to Eq. (4), while the macroscopic contact angle is the result of the surface shape (see Appendix C). This simulation study shows that the model is able to maintain the theoretical macroscopic contact angle in the three-phase region under dynamic conditions of a moving fluid interface. In addition, a convergence can be observed, which indicates that the numerical error decreases with higher resolution.

B. Rise of a fluid in a capillary

Setup and parameters. In this section, the capillarity between two fluids in a riser of width r is investigated. As a benchmark quantity, the filling height h relative to the fluid interface at mechanical equilibrium is evaluated (see Appendix A). The corresponding analytical solution is given by the equation

$$\hat{h} = \frac{h}{r} = \left(\frac{\sigma \cos(\Theta)}{\rho g} - A\right)\frac{1}{r^2}, \tag{17}$$

with nondimensionalized height $\hat{h}$, surface tension σ, contact angle $\Theta = 180^\circ - \theta$, density ρ of fluid 2, and gravity g. Details on the derivation for the analytical solution and the definition of the area A can be found in Appendix A. Figure 3 shows the initial setup. Due to the symmetry, only half of the riser is calculated, taking into account the physical dimensions of the system, $l_x = 10.0 \times 10^{-3}$ m and $l_y = 55.0 \times 10^{-3}$ m, and a riser width of $r = 0.15 \times 10^{-3}$ m. It is placed in a reservoir filled with water, represented by fluid 2 φ_2 with density $\rho_2 = 997.0\ \mathrm{kg\,m^{-3}}$ and viscosity $\mu_2 = 1.0 \times 10^{-3}$ Pa s. In addition, the surrounding fluid 1 φ_1 mimics air with a density of $\rho_1 = 1.225\ \mathrm{kg\,m^{-3}}$ and a viscosity of $\mu_1 = 1.72 \times 10^{-5}$ Pa s. The contact angle is given by $\theta = 120^\circ$, with a surface tension of $\sigma = 7.3 \times 10^{-2}\ \mathrm{N\,m^{-1}}$. To validate the model, a grid refinement study is first carried out for a specified Bond number ($\mathrm{Bo} = 3.35 \times 10^{-2}$), which is defined as

$$\mathrm{Bo} = \frac{\rho g l_{\mathrm{char}}^2}{\sigma}, \tag{18}$$

with a characteristic length of $l_{\mathrm{char}} = r$ for the present case. While maintaining the physical domain size, simulations are performed with three different numerical resolutions, where the corresponding numbers of cells in the x and y directions are 100×550, 200×1100, and 400×2200. In addition, for the coarse resolution of 100×550 cells, the Bond number is varied by changing the gravity g.

Results. Figure 4 shows the determined riser height $\hat{h}$ as a function of the Bond number Bo. In addition, the grid refinement study for a Bond number of $\mathrm{Bo} = 3.35 \times 10^{-2}$ is depicted as an inlet picture. For both studies, the analytical solutions are marked by a brown line. The simulation results for the grid refinement study are $\hat{h} = 14.0$, $\hat{h} = 14.27$ and $\hat{h} = 14.33$ for the cell numbers 100×550, 200×1100 and 400×2200, respectively. Using the analytical solution $\hat{h}^{\mathrm{anal}} = 14.841$ the relative errors, defined by $\epsilon = (\hat{h}^{\mathrm{anal}} - \hat{h})/\hat{h}^{\mathrm{anal}}$, are $\epsilon = 5.56\,\%$, $\epsilon = 3.85\,\%$ and $\epsilon = 3.44\,\%$. It follows that for a better grid refinement, the analytical solution is mapped more accurately, as the numerical error is reduced. This proves the convergence and successfully verifies the numerical solution. The simulated results for different Bond numbers for the cell numbers $n_x \times n_y = 100 \times 550$ are depicted as black dots in Fig. 4 illustrating that the model approximates the analytical solution well for all simulated Bond numbers.

C. Channel grid

In this section, the influence of different pore sizes on pore emptying during drying is analyzed. The simulation parameters are identical to those from Sec. III A, with the exception of the contact angle, which for this study is $\theta = 90^\circ$. A resolution of 480×480 with a physical domain size of $l_x = 56.0\,\mu\mathrm{m}$ and $l_y = 56.0\,\mu\mathrm{m}$ is used. Three different configurations, which are shown in Fig. 5, are considered. These configurations differ in the pores that are located horizontally and vertically in the center of the simulation area. Starting from the reference configuration, which is depicted on the left in Fig. 5, the pores located in the horizontal and vertical center are enlarged for the second configuration (center) by removing rectangles. For the third configuration (right), the vertical pore is enlarged by further removing rectangles. This approach allows the simulation of different pore size distributions and the subsequent analysis of their effects during the drying process, in analogy to the setup used in Fig. 4.17 of [71]. The bottom row of Fig. 5 shows the different configurations at the time of breakthrough, which indicates the point at which the air reaches the bottom of the system. For the reference configuration, it can be observed that the liquid evaporates mainly into the larger pores, but also into the smallest pores. In the second configuration, which has larger pores in the horizontal and vertical center, the liquid evaporates preferentially into these pores. Additionally, the liquid begins to evaporate in the next smaller pores, while the smallest pores are still filled in this configuration. For the last configuration, the result is similar to the other configurations, with the larger pores emptying first,

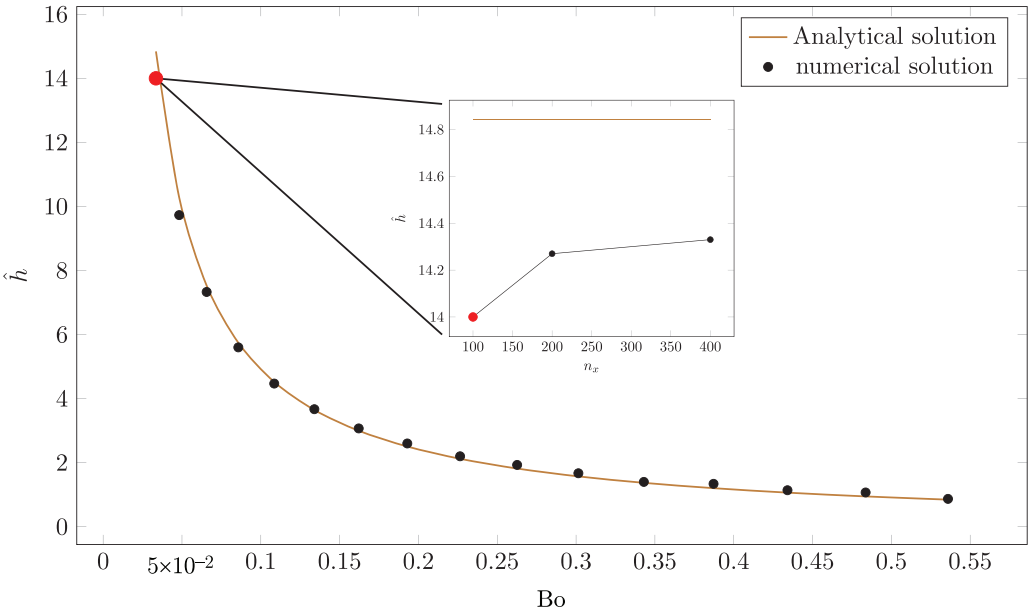

FIG. 4. Rise of a liquid in a capillary: Dimensionless rise height $\hat{h}$ versus the Bond number for simulation results and the analytical solution. Additionally, the effect of the grid refinement n_x on the rise height $\hat{h}$ is shown as an inlet at a specific Bond number of Bo = 0.05.

followed by the smaller pores. In contrast to the other configurations, pinning of the liquid at the original fill level can be observed. In summary, it can be said that large capillaries empty first before smaller capillaries, which is consistent with the findings from the literature [41]. The possibility of pinning on the surface is given, which has also been observed in the drying of battery electrodes [8], and can be described analytically for a two-capillary system [72]. This pinning is reflected in a height difference between a continuous line connecting the highest and lowest positions of the liquid and will be used as a parameter for the subsequent analysis. Wrapping up, the result of this simulation study shows the expected behavior indicating that the present model is suitable to predict pore emptying processes.

IV. APPLICATION OF THE MODEL TO THE DRYING OF HARD CARBON ELECTRODES FOR BATTERIES

In this section, the drying of the solvent of battery electrodes is simulated using the proposed model. Herein, the

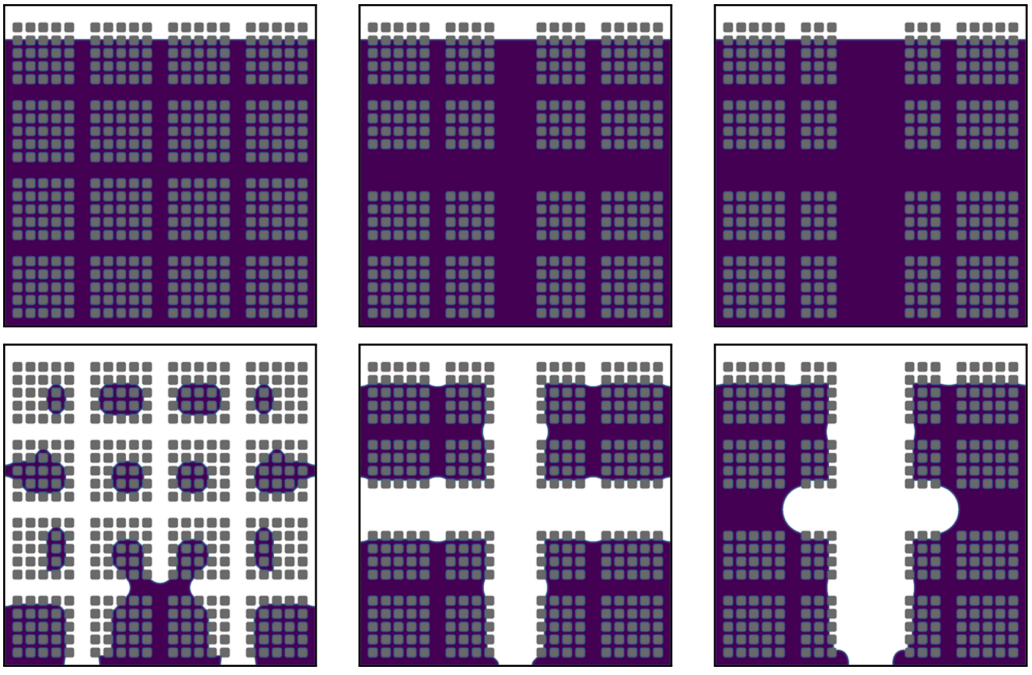

FIG. 5. Simulation results for different pore structures, with the initial condition in the top row and time of breakthrough in the bottom row. The fluids, referred to as fluid 1 (air) and fluid 2 (liquid), are shown in white and blue, respectively. The solid phase is displayed in gray.

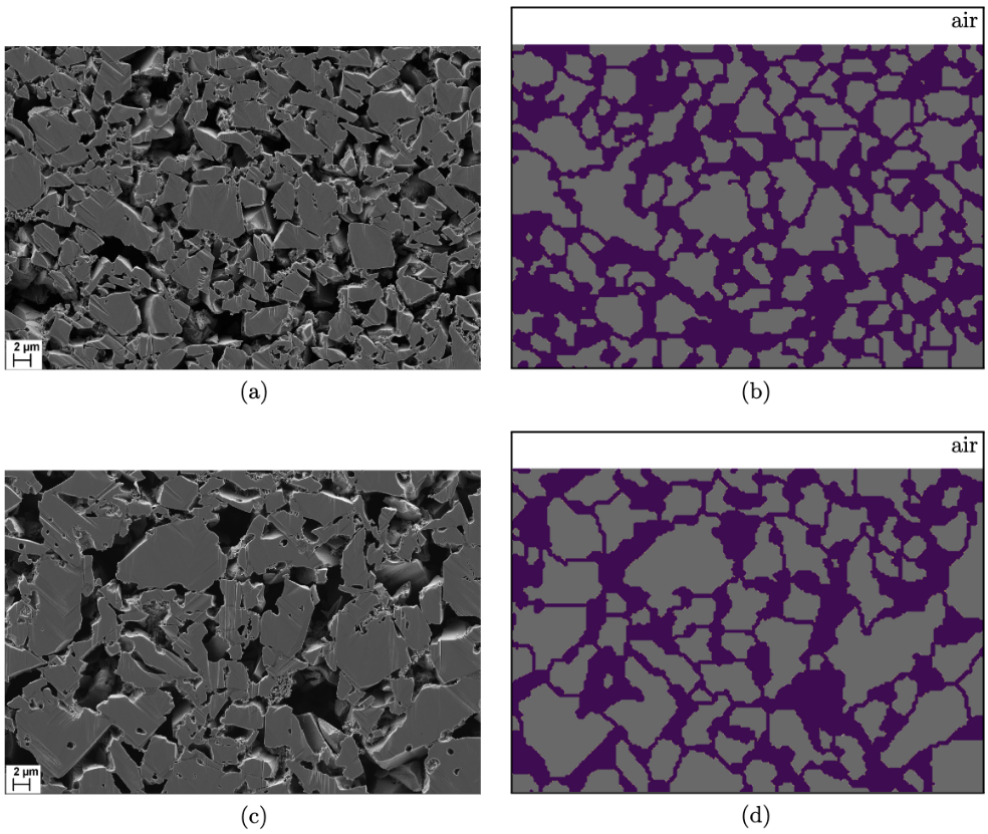

FIG. 6. Microstructures of hard carbon [16] with different mean particle diameters and pore size distributions as well as the corresponding initial microstructures for the simulations. (a) SEM image of microstructure HC-B. (b) Initial simulation input for microstructure HC-B. (c) SEM image of microstructure HC-C. (d) Initial simulation input for microstructure HC-C.

drying is modeled as a convective capillary flow, while transport phenomena of the evaporated liquid in the gas phase are excluded. The influence of viscosity on the drying process is investigated for two different microstructures. In addition, the effect of different contact angles on pore emptying is investigated for one representative microstructure.

A. Preprocessing and simulation setup

Microstructures. The simulations are performed on the basis of two images of dried hard carbon electrodes. These are integrated into the simulation environment, with the help of a Kadi4Studio workflow [73] and an imagej macro. Figure 6 shows the two different microstructures from Klemens *et al.* [16] with the corresponding microstructures as input for the simulations. For a better readability, the names HC-B and HC-C are adapted accordingly. Microstructure HC-B has a smaller average particle diameter and a less broad pore and particle size distribution than microstructure HC-C. Furthermore, microstructure HC-B is defined by a specific area weight of $M_S = 78.4 \times 10^{-3}\,\mathrm{kg\,m^{-2}}$ and a volume fraction of $\chi_{solid} = 0.246$, while microstructure HC-C has the values $M_S = 79.5 \times 10^{-3}\,\mathrm{kg\,m^{-2}}$ and $\chi_{solid} = 0.245$. The physical lengths of the microstructures are $l_x = 55.0\,\mu\mathrm{m}$ and $l_y = 37.5\,\mu\mathrm{m}$. In order to take the initial air layer into account, the computational domain is extended in preprocessing, considering a domain height of $l_y = 42\,\mu\mathrm{m}$.

Parameters. The material parameters for the solvent are selected with $\rho_{solvent} = 997.0\,\mathrm{kg\,m^{-3}}$ for the density and $\mu_{solvent} = 1.0\,\mathrm{Pa\,s}$ for the viscosity. It should be noted that due to the thickener carboxymethyl cellulose (CMC), the viscosity differs from the viscosity of water and is chosen according to the literature [74]. Both the fluid and the battery slurry are shear thinning [16], which can be modeled with a rate-dependent viscosity and thus a generalized Newtonian behavior. Subsequently, in the present model all fluids are considered Newtonian fluids for the sake of simplicity. Regarding the air phase, a density of $\rho_{air} = 1.225\,\mathrm{kg\,m^{-3}}$ and a viscosity of $\mu_{air} = 1.72 \times 10^{-5}\,\mathrm{Pa\,s}$ are assumed. As the density interpolation may become unstable at high density ratios (cf. [75]), the air density is artificially increased by a factor of 4 for the subsequent simulations to prevent instability. A surface tension between the different fluids of $\sigma = 7.3 \times 10^{-2}\,\mathrm{N\,m^{-1}}$ with a contact angle of 90° is applied. Furthermore, the gravity is set to $g = 9.81\,\mathrm{m\,s^{-2}}$. The mobility is defined by $M = 30.0\,\mathrm{m\,s\,kg^{-1}}$, whereby an area-specific evaporation rate of $\dot{r}_{solvent} = 9\,\mathrm{g\,m^{-2}\,s^{-1}}$ is used, which is chosen relatively high in the context of film drying [3] to avoid excessive simulation times. All physical parameters can be found in Table I. For the cell numbers the values $n_x = 592$ and $n_y = 448$ are used, leading to the dimensionless spatial step sizes of $\Delta x^* := \Delta x / l_{char} = 1.69 \times 10^{-3}$ and $\Delta y^* := \Delta y / l_{char} = 1.70 \times 10^{-3}$, respectively, with the characteristic length scale $l_{char} = l_x = 55.0\,\mu\mathrm{m}$.

TABLE I. Overview of the simulation parameters for hard carbon microstructures.

Parameter	Symbol	Physical value	Unit
physical length	l_x	55.0	µm
physical height	l_y	42.0	µm
density hard carbon	ρ_{HC}	2069.0	kg m^{-3}
density solvent	$\rho_{solvent}$	997.0	kg m^{-3}
density air	ρ_{air}	1.225	kg m^{-3}
viscosity solvent	$\mu_{solvent}$	1.0	Pa s
viscosity air	μ_{air}	1.72×10^{-5}	Pa s
surface tension	σ	7.3×10^{-2}	N m^{-1}
gravity	g	9.81	m s^{-2}
mobility	M	30	m s kg^{-1}

Dimensional analysis. Using the parameters from Table I, a nondimensionalization analysis is performed. In addition, the characteristic velocity is described by $u_{char} = \dot{r}_{solvent}/\rho_{solvent} = 9.03 \times 10^{-6}$ m s^{-1}. This results in the relevant dimensionless variables $Bo_s = 4.48 \times 10^{-4}$, $Ca_s = 1.37 \times 10^{-4}$, $Re_s = 4.95 \times 10^{-7}$, $Bo_a = 5.51 \times 10^{-7}$, $Ca_a = 2.4 \times 10^{-9}$, and $Re_a = 3.54 \times 10^{-5}$ for the solvent and air.

To enable short simulation times, we use the approach of Wolf *et al.* [22] and scale the physical problem. For this, the drying rate is corrected upward by the factor 5.0×10^4, while the viscosity of the two fluids present is scaled downward by the same factor. This results in a constant capillary number, which represents the ratio of viscous forces to capillary forces and is defined later. With this approach, the computational time for drying the hard carbon electrodes is approximately one to two days, using the hardware specified in Sec. II.

Various parameters are used to evaluate the simulation results. These are controlled by pore breakthroughs, which have also been observed in experiments [11] and are defined by the breakthrough of the air onto the substrate. First, the nondimensionalized time ($t^{breakthrough}$) of the breakthrough is evaluated. The physical time can be calculated according to $t^{physical} = t t_{char}$, with $t_{char} = l_{char}/u_{char} = 6.0928$ s as the characteristic time, and t as the nondimensionalized time. Thereby a drying time of approximately 6.9075 s is achieved for the pore emptying, with an evaporation rate of 9 g m^{-2} s^{-1}, which can be achieved experimentally [16]. Furthermore, the height difference, denoted as Δh, is examined at the breakthrough time ($t^{breakthrough}$), as shown in the inset picture in Fig. 7(a). The height difference is defined as the maximum difference

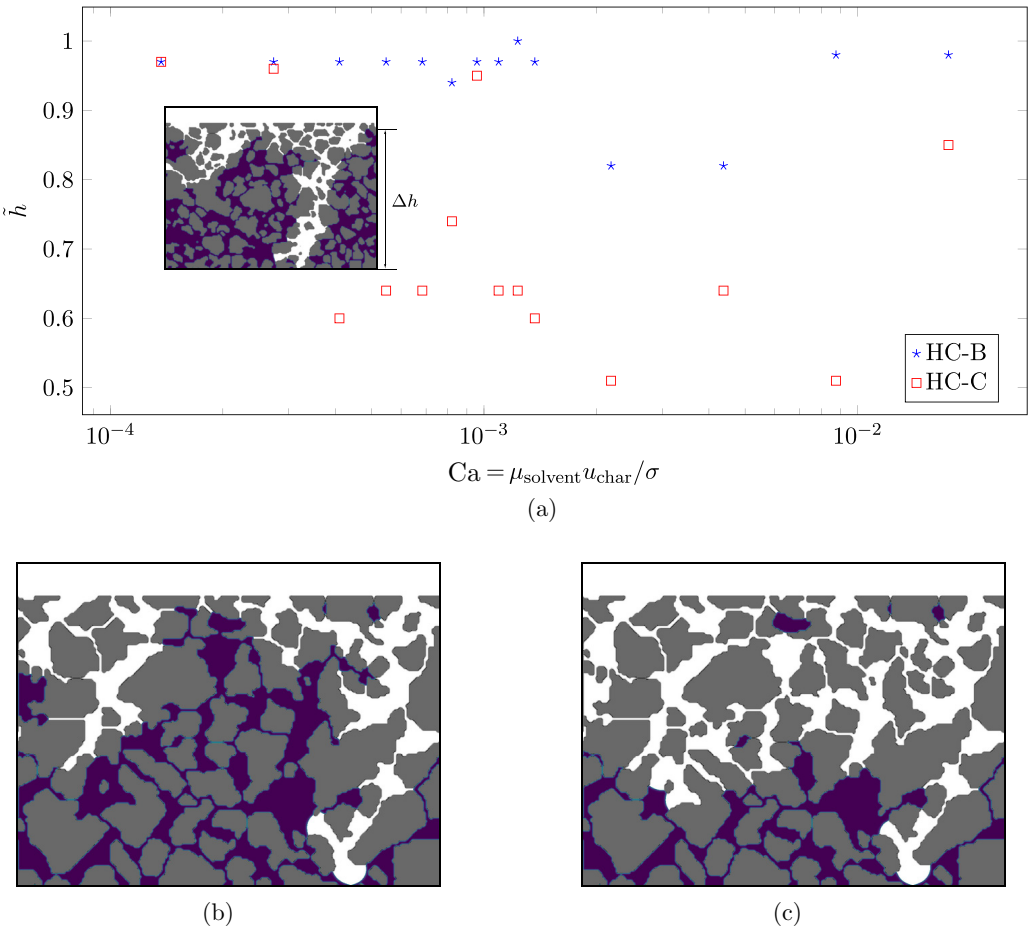

FIG. 7. Top: Dependence of the normalized height difference $\tilde{h}$ of the breakthrough point on the capillary number Ca. (a) Simulated normalized height difference $\tilde{h}(= \Delta h/h'^{=0}_{film})$ of the film, as a function of the capillary number Ca, for two microstructures. The blue and red symbols refer to microstructures HC-B and HC-C, respectively. Bottom: Microstructure images of simulations for selected combinations of capillary number and nondimensionalized breakthrough time. (b) HC-C ($Ca = 1.368 \times 10^{-4}$) at $t^{breakthrough} = 0.4736$. (c) HC-C ($Ca = 2.188 \times 10^{-3}$) at $t^{breakthrough} = 0.7702$.

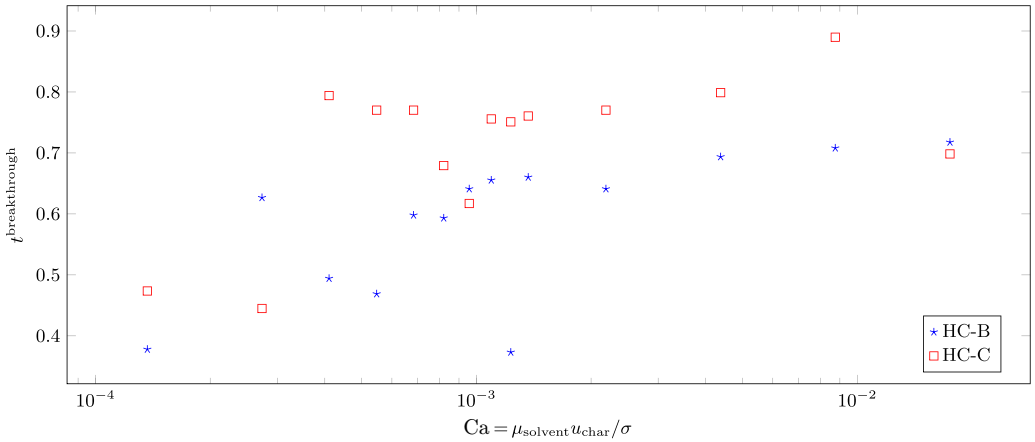

FIG. 8. Nondimensionalized breakthrough time $t^{\text{breakthrough}} = t^{\text{physical}}/t_{\text{char}}$, as a function of the capillary number Ca. Microstuctures HC-B and HC-C are shown in blue and red, respectively.

between y-coordinates of the solvent front, which are continuously connected to each other and thus enable the capillary transport of solvent and binder. For further evaluation, the height difference is normalized to the initial film height $h_{\text{film}}^{t=0}$ and the corresponding abbreviation $\tilde{h} = \Delta h/h_{\text{film}}^{t=0}$ is introduced. Another parameter that is examined is the normalized $\hat{x}$-coordinate, which specifies the x-coordinate of the breakthrough normalized by l_x. Simulations results are evaluated in relation to the capillary number

$$Ca = \frac{\mu_{\text{solvent}} u_{\text{char}}}{\sigma}. \tag{19}$$

B. Variation of the capillary number

Height difference of the liquid front. Figure 7(a) shows the normalized difference between the maximum height and the minimum height at the time of breakthrough onto the substrate as a function of the capillary number. For microstructure HC-B the results are displayed in blue, while the results for HC-C are plotted in red. In the case of microstructure HC-B, it can be seen that for most cases, with the exception of the capillary numbers $\text{Ca} = 2.188 \times 10^{-3}$ and $\text{Ca} = 4.377 \times 10^{-3}$, the normalized height difference is approximately $\tilde{h} = 0.97$. So there are still places where a solvent column reaches the film height, whereas otherwise columns have fallen dry depending on their shape and diameter. For the capillary numbers $\text{Ca} = 2.188 \times 10^{-3}$ and $\text{Ca} = 4.377 \times 10^{-3}$, the normalized height difference is $\tilde{h} = 0.82$. The behavior for microstructure HC-C differs from that of the other microstructure. In general, the scatter of the values for $\tilde{h}$ is higher than for microstructure HC-B. At a capillary number of $\text{Ca} = 4.104 \times 10^{-4}$, the value for the normalized height difference drops to approximately $\tilde{h} = 0.64$ and scatters around this value. An exception to this are the capillary numbers $\text{Ca} = 9.576 \times 10^{-4}$ and $\text{Ca} = 1.751 \times 10^{-2}$ with the values $\tilde{h} = 0.94$ and $\tilde{h} = 0.85$, respectively. Figures 7(b) and 7(c) show microstructure images of the solvent distribution at the time of breakthrough for the capillary numbers $\text{Ca} = 1.368 \times 10^{-4}$ and $\text{Ca} = 2.188 \times 10^{-3}$ of microstructure HC-C. Comparing the two snapshots, a different behavior can be observed. In Fig. 7(b), the liquid front pins much closer to the microstructure surface than in Fig. 7(c). Similar pinning on the film surface is also reported in other simulation studies [43] as well as in experiments [10,14] and is based on the capillary forces acting in a pore system. Whether pinning occurs depends on the viscosity and the pore size distribution of the microstructure [43]. While capillary forces transport the liquid to the surface during drying, this effect is counteracted by the damping forces of viscosity. Therefore, the difference in the behavior observed in Fig. 7(a) can be explained by the dependence on the capillary number. If the capillary number increases due to a higher viscosity of the liquid, the damping forces increase. Thus, the probability of transport to the surface decreases. In general, the solvent in microstructure HC-B is more likely to pin to the top of the film, compared to the HC-C microstructure, due to the narrow pore size distribution, which is also reported by Metzger *et al.* [41,42]. Moreover, microstructure HC-C shows a wider scatter for the normalized height as a result of a wider pore size distribution that allows for more capillary veins.

Breakthrough time. Figure 8 displays the time of breakthrough as a function of the capillary number for the two different microstructures HC-B and HC-C, with blue and red symbols. A similar relationship between capillary number and breakthrough time is found for both microstructures, with most breakthrough times increasing with higher capillary numbers. Furthermore, the breakthrough times of microstructure HC-C are mostly greater than for microstructure HC-B, except for the capillary numbers $\text{Ca} = 2.736 \times 10^{-4}$, $\text{Ca} = 9.576 \times 10^{-4}$, and $\text{Ca} = 1.751 \times 10^{-2}$. From the literature (see, e.g., [43,44]) a monotonic increase of the breakthrough time with the capillary number is expected, since a higher viscosity dampens the speed of the capillary-driven solvent flow. This reduces the probability that a specific pore will break through to the substrate prior to others. Specifically, in the limiting case of $\text{Ca} \to \infty$, a horizontal liquid front is expected during evaporation. The overall trend is reflected by Fig. 8, where the breakthrough time increases for higher capillary numbers. However, this trend is not strictly monotonic in the present results. In order to explain these nonmonotonic variations in the results, the temporal development of microstructure HC-B for the capillary numbers $\text{Ca} = 1.368 \times 10^{-4}$, $\text{Ca} = 2.736 \times 10^{-4}$, and $\text{Ca} = 4.104 \times 10^{-4}$

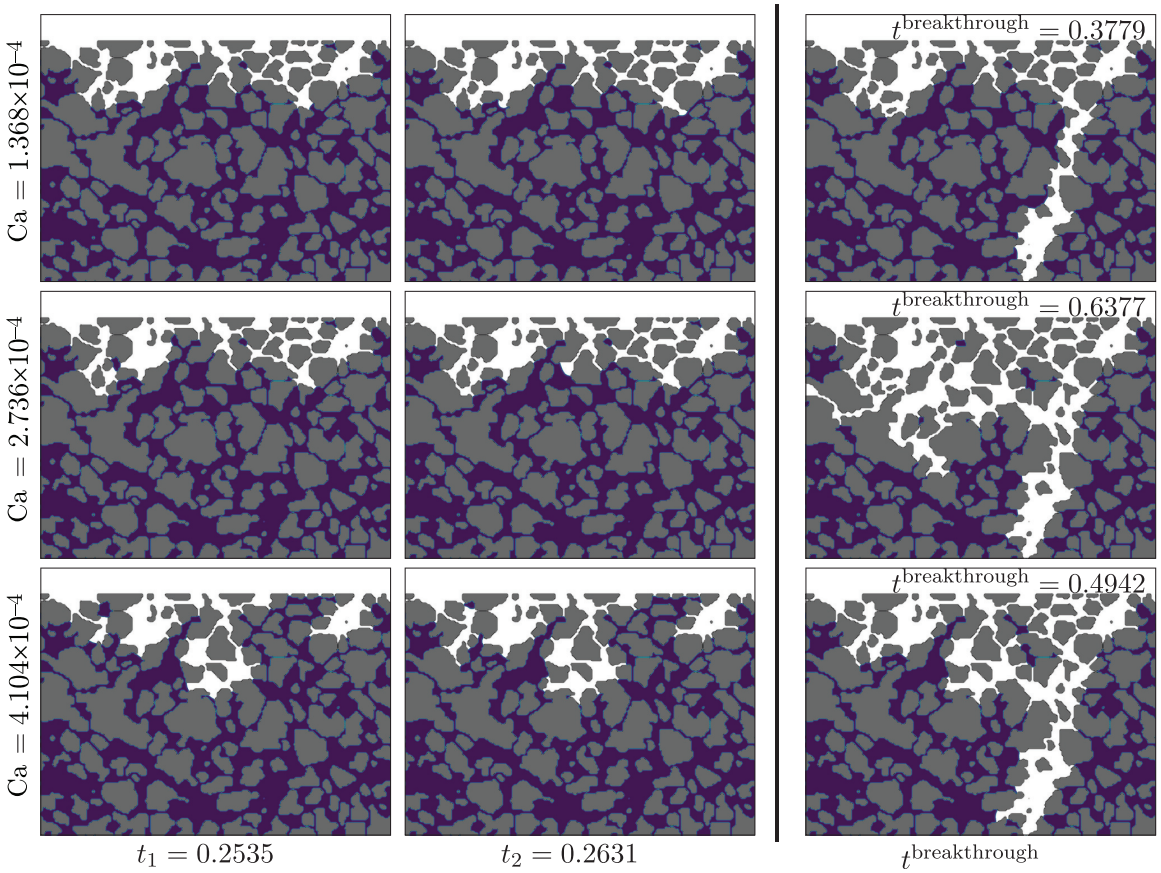

FIG. 9. Temporal evolution of microstructure HC-B for different capillary numbers Ca, at fixed times $t_1 = 0.2535$, $t_2 = 0.2631$, and measured nondimensionalized breakthrough times: $t^{\text{breakthrough}} = 0.3779$, $t^{\text{breakthrough}} = 0.6377$, and $t^{\text{breakthrough}} = 0.4942$ for $\text{Ca} = 1.368 \times 10^{-4}$, $\text{Ca} = 2.736 \times 10^{-4}$, and $\text{Ca} = 4.104 \times 10^{-4}$. The air and solvent particles are shown in white, blue, and gray, respectively.

is examined more closely as an example. Figure 9 includes the simulation results for three different points in time, labeled t_1, t_2, and $t^{\text{breakthrough}}$, for the mentioned capillary numbers. The two fluids and particles are visualized in white (air), blue (solvent), and gray (particles), respectively. At time t_1, the pore emptying is almost identical for the capillary numbers $\text{Ca} = 1.368 \times 10^{-4}$ and $\text{Ca} = 2.736 \times 10^{-4}$, while for $\text{Ca} = 4.104 \times 10^{-4}$, the location of the liquid front is already different. This is also the case for the capillary numbers $\text{Ca} = 1.368 \times 10^{-4}$ and $\text{Ca} = 2.736 \times 10^{-4}$ at time t_2. For a value of $\text{Ca} = 2.736 \times 10^{-4}$, a temporally limited pinning of the solvent in the capillary occurs in the right-hand area of the microstructure, which is not observed at a capillary number of $\text{Ca} = 1.368 \times 10^{-4}$. The effect of this pinning can be seen at the breakthrough time $t^{\text{breakthrough}}$ for the capillary numbers $\text{Ca} = 2.736 \times 10^{-4}$ and $\text{Ca} = 4.104 \times 10^{-4}$, where the breakthrough time is higher for the lower capillary number, contrary to the expected behavior. Wrapping up these observations, the nonmonotonic variations in the breakthrough time are caused by locally different pinning effects in specific capillary veins, which can temporarily stop the height reduction within a certain capillary of the microstructure. Furthermore, it can be observed that, due to this pinning behavior, different breakthrough paths can be preferred, as indicated by different x coordinates of the breakthrough point, where the air reaches the substrate first (see Appendix F). Therefore, the breakthrough time is not only influenced by the speed in the capillary, but also by the length of the breakthrough path that is taken. The pinning effects are influenced by the capillary number, the microstructure geometry, and the history of the liquid front, which in total illustrates the influence of local effects arising from the microstructure. It is to be noted that a single realization of a microstructure, as considered in this work, cannot cover the statistics of a larger ensemble. Therefore, an ensemble of microstructures with the same characteristics can be used for averaging the evaluation parameters like the breakthrough time. With this statistical evaluation we would expect monotonic behavior of the curves using the ensemble averages.

Summary. In this section, pore emptying is investigated under a number of boundary conditions. These boundary conditions are the viscosity and the property of the microstructure, which is not only considered by statistical parameters. It is shown that the effective capillary leading to breakthrough depends on the capillary number and the microstructure properties. Here, the effective capillary refers to the path of the liquid front up to the breakthrough. The height difference of the liquid front, which describes the pinning on the surface of a pore structure, is also dependent on these parameters. Outliers in the simulation results could be attributed to other effective capillaries found in the microstructure. A comprehensive understanding of such behavior is only possible due

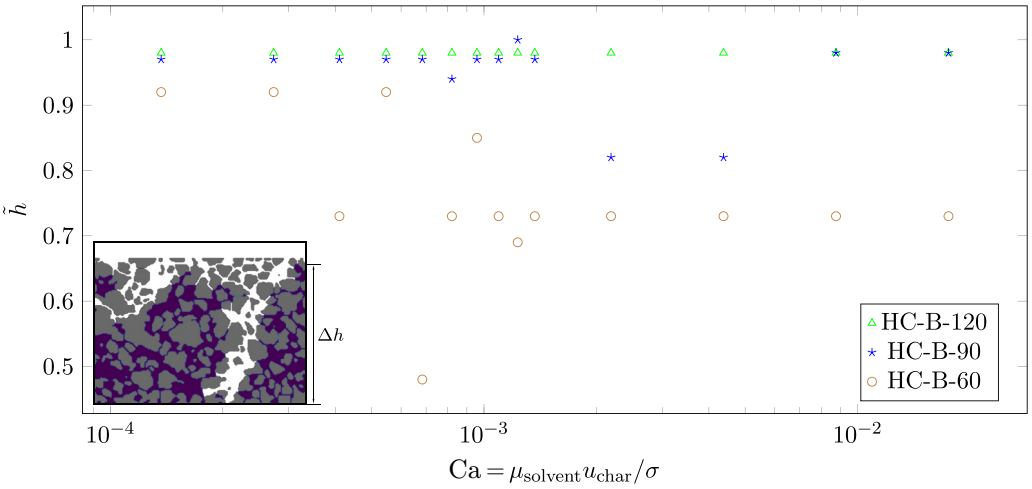

FIG. 10. Dependence of the normalized film height $\tilde{h}$ on the capillary number for different contact angles at the time of breakthrough. The contact angles 60°, 90°, and 120° are shown in brown, blue, and green.

to the information provided by the developed model across the entire field. This includes the phase-field variable, which enables a precise representation of the solvent over time. In summary, computational modeling provides novel insights into the microstructural properties and developments during the drying process of battery electrodes.

C. Variation of the contact angle

While in the previous section a neutral wettability and thus a contact angle of 90° is assumed, the effect of a change in the contact angle is subsequently investigated. There are studies investigating the impact of wettability and contact angle in two-dimensional (2D) porous media under conditions of minimal evaporation [46,47]. These studies suggest a significant effect of wettability, which should also be considered in the context of drying of battery electrodes. Since the model used in the present work can cover wetting effects, the impact of the contact angle during the drying process is accessible. For this purpose, the results with a contact angle of 90° are compared with contact angles of 60° and 120°, which indicate hydrophobic and hydrophilic behavior, respectively.

Figure 10 illustrates the effect of the contact angle on the normalized height difference $\tilde{h}$ as a function of the capillary number Ca. The different angles 60°, 90°, and 120° are shown as symbols in the colors brown, blue, and green, respectively. For a contact angle of 120°, no dependence of the height on the capillary number can be seen, whereas the values for a contact angle of 60° and 90° are scattered. All values for a contact angle of 60° are smaller than the values for the other contact angles. Without taking into account the capillary number $\mathrm{Ca} = 1.231 \times 10^{-3}$, this behavior is also evident between the contact angles 90° and 120°. Here, the results are either identical or the values for a contact angle of 90° are lower than those for 120°. Compared to the results for an angle of 90°, however, the results for an angle of 60° are more widely distributed and depend on the capillary number. This parameter study indicates that, as the contact angle decreases, the pinning on the surface is less pronounced; following that the normalized height difference is smaller. Such a behavior leads to a more uniform drying front with a decreasing contact angle, while at the same time the values are more scattered. While a constant value is obtained at a contact angle of 120°, a large scatter is observed at a contact angle of 60°. Figure 11 shows the time of breakthrough for the three different angles, which are represented in brown, blue, and green symbols for the angles 60°, 90°, and 120°, as a function of the capillary number Ca. The behavior of the breakthrough times is different for all three contact angles. In addition, the distribution of the data points assigned to the three different contact angles differs in the scattering property, with the variation being less pronounced at larger contact angles. At a contact angle of 120°, the breakthrough time is almost constant over Ca.

A qualitative comparison of Chraibi *et al.* [47] shows similar behavior. Therein, larger breakthrough times are observed, the more hydrophobic the material is, which agrees with the present results. In addition, the order of magnitude in change of the breakthrough times for different wettability is similar in both studies. However, a quantitative comparison is not possible due to the different microstructure characteristics with regard to the pore size distribution and porosity. Wrapping up, the simulation studies point out that the contact angle plays an important, non-negligible role for pore emptying during the drying of battery electrodes. Furthermore, a tailored regulation of the contact angle offers potential for optimizing the drying process. This can be achieved by a special treatment of the particle surface, for example, by altering the surface structure.

D. Discussion of the simplifying assumption

Both the model and the problem setup for the film drying simulations are based on assumptions and simplifications that are critically discussed in the following section, while possible paths for future developments are identified.

Navier-Stokes equations. A constant viscosity is chosen for the fluid, which represents the solvent and the additives. However, in general, the viscosity depends on the temperature and the shear rate. In particular, the dependence of the viscosity on the shear rate is well known in the drying of battery

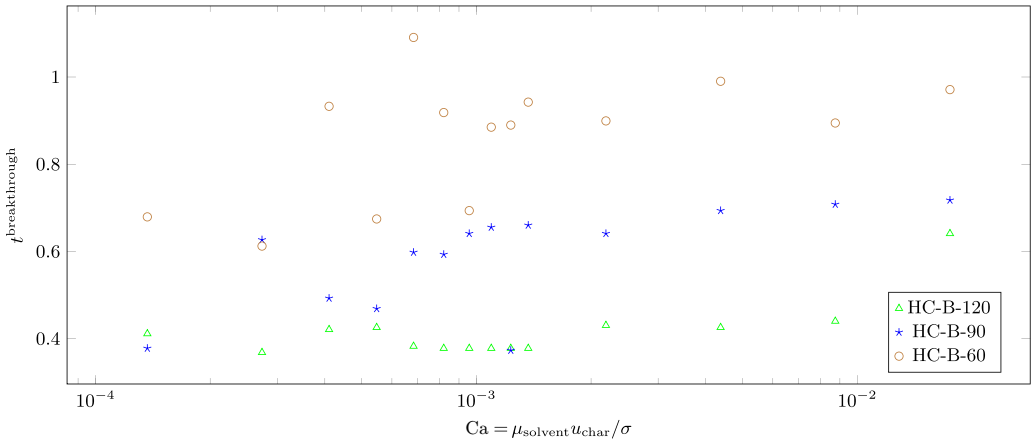

FIG. 11. Nondimensionalized breakthrough time $t^{\text{breakthrough}} = t^{\text{physical}}/t_{\text{char}}$, as a function of the capillary number Ca, for different contact angles.

electrodes [16]. This dependence can be introduced by defining the shear rate $\dot{\gamma} = \sqrt{4I_2(\boldsymbol{D})}$ based on the second basic invariant $I_2 = \text{tr}(\boldsymbol{DD})$ of the symmetric velocity gradient $\boldsymbol{D}$. For such an approach, it is necessary to model the viscosity as a function of the shear rate, $\mu = \mu(\dot{\gamma})$, which can be achieved by using a power law, for example (cf. [59]).

Interpolation. In the simulations, the density of the air phase is four times higher than the real air density. This is due to the fact that the interpolation of the physical parameters in the diffuse interface can lead to problems with high contrasts between the phases [75]. The scaling can be justified by dimensional analysis. The very small Reynolds and Weber numbers regarding the air phase indicate that only minimal inertia effects are present, which is also the case after scaling. Therefore, the effect of the air velocity on the movement in the solvent is negligible, while the movement in the solvent is the relevant feature to be covered by the simulations. Similarly, the air stream utilized for drying is not included in the problem setup, which is a widely used simplification [22]. To solve the density interpolation problem, a model extension can be made by adding another term to the Navier-Stokes equation that accounts for the momentum exchange due to molecular diffusion, as proposed by Abels *et al.* [75].

Evaporation. In the proposed model, the evaporation rate is modeled as a constant value. Furthermore, the evaporation rate is evenly distributed over the diffuse interface. In reality, the saturation of the gas phase in the pores reduces the driving force for diffusive solvent transport in the gas phase, and the local evaporation rate can change. One way to describe the drying rate $\dot{m}_{\text{S}}$ is according to [10]

$$\dot{m}_{\text{S}} = \tilde{M}_{\text{S}} \tilde{\rho}_{\text{G}} \gamma_{\text{S,G}} \ln \frac{(1 - \tilde{\gamma}_{\text{S},\infty})}{(1 - \gamma_{\text{S,Ph}})}, \tag{20}$$

where $\tilde{M}_{\text{S}}$ is the molar mass of the solvent, $\tilde{\rho}_{\text{G}}$ represents the molar density of the surrounding gas stream, $\beta_{\text{S,G}}$ is the mass transfer coefficient, $\tilde{\gamma}_{\text{S},\infty}$ is the molar fraction of the solvent in the drying air, and $\gamma_{\text{S,Ph}}$ denotes the molar fraction of the solvent in the solvent-gas interface. This requires an additional transport equation that takes into account the solvent concentration in the gas phase. As some of the parameters, such as the molar fractions, depend on the temperature, the temperature must also be taken into account.

The simplifications in the current work can be addressed by incorporating extensions to the discussed model, thereby enhancing the accuracy of the results. Despite these simplifications, the presented model covers the most relevant physical effects for pore emptying during drying and requires fewer assumptions, compared to other models used to simulate film drying.

V. SUMMARY AND OUTLOOK

In this work, a full-field approach to simulate pore emptying in battery electrode drying is presented. This approach builds on the model proposed by Reder *et al.* [54] and applies an Allen-Cahn approach as an alternative to the Cahn-Hilliard approach. Additionally, this approach takes into account the phase transition due to evaporation. The model is validated using three different examples, which concern the macroscopic contact angle behavior during evaporation, the rise height of a fluid in a capillary, and the behavior of an evaporating fluid in a pore network. With respect to all validation cases, the model shows good agreement with the theoretical predictions. Subsequently, the influence of the contact angle, viscosity, and microstructure on the drying behavior is investigated using realistic hard carbon microstructures as initial conditions. For both microstructures, a correlation between viscosity and breakthrough time can be derived, which consists of the fact that the time to breakthrough also increases with increasing viscosity. However, this correlation can be negated as a result of the existence of privileged capillaries, by changing the contact angle. In addition, it can be noted that the breakthrough time increases for hydrophobic behavior and decreases for hydrophilic behavior. Concurrently, the influence of the capillarity number on the breakthrough time decreases with an increase in hydrophilic behavior. Overall, a stabilization of the liquid front can be achieved both by increasing the viscosity and by a more hydrophobic behavior, which is known from other studies as well [47]. Thereby, the influence of the surface wettability on the breakthrough time and, consequently, the stabilization of the liquid front is more significant in the parameter range considered in the

present work. Two conclusions can be drawn from the studies: first, that models which model the drying of battery electrodes should take the studied parameters into account, and second, the production of battery electrodes can be optimized by changing the contact angle due to surface optimization. A subsequent study will be conducted in order to investigate the influence on more complex microstructures like multilayer microstructures or three-dimensional (3D) microstructures. In particular, the simulation of 3D microstructures is important to determine the statistical effects of 2D structures and to correctly map the complexity of effective capillaries in all three spatial directions. Besides the use of 3D microstructures, ensembles of several microstructure realizations will be used in future studies to increase statistical representation. Furthermore, experimental measurements of breakthrough times for film drying are possible using microscopy of drying battery electrodes coated on a glass substrate (cf., for example, [[11]. Currently, no such data are available for hard carbon electrodes, but conducting such experiments and a comparison with the present simulation can be addressed in future work. Additionally, the model can be easily extended to evaluate the binder behavior under drying conditions, since the full-field information of the solvent velocity is already known. For this purpose, a diffusion-convection equation needs to be integrated into the model. We hope that these extensions will allow us to better understand and optimize the drying of battery electrodes.

ACKNOWLEDGMENTS

This work contributes to the research performed at CELEST (Center for Electrochemical Energy Storage Ulm-Karlsruhe) and was funded by the German Research Foundation (DFG) under Project ID 390874152 (POLiS Cluster of Excellence). Within the cooperation of the cluster we thank Dr. Marcus Müller (Institute for Applied Materials IAM-ESS) for support regarding the SEM measurements. Support regarding the model development is provided through funding by the Helmholtz association within the programme "MTET" (No. 38.02.01), which is gratefully acknowledged.

The authors declare no conflict of interest.

DATA AVAILABILITY

The data that support the findings of this article are openly available [76].

APPENDIX A: CALCULATION OF THE HEIGHT OF A CAPILLARY

The forces acting in a capillary are shown in Fig. 12. The height of rise, h, in the capillary in steady state can be calculated using a force balance. Thus, the gravitational force F_g and the force F_σ due to the surface tension on the wall balance each other out. The gravitational force is described by the relationship

$$F_g = (\rho_2 - \rho_1)gV, \tag{A1}$$

where ρ_2 is the density of fluid 2 and ρ_1 is the density of fluid 1. V denotes the volume of fluid 2 and g describes the

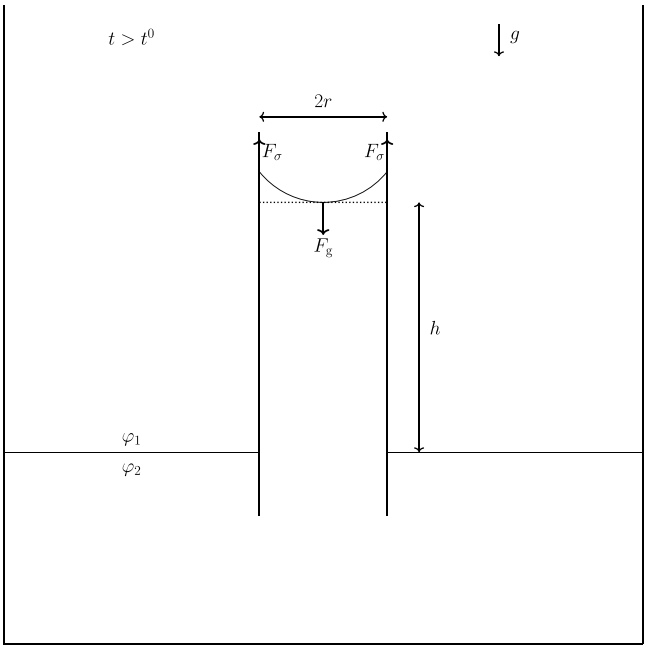

FIG. 12. Balance of forces for a capillary.

acceleration due to gravity. The surface tension force is given by

$$F_\sigma = \sigma \cos\Theta D, \tag{A2}$$

where D represents the depth and Θ is the contact angle. The volume $V = AD$ of the liquid φ_2 is given with the surface A of fluid 2, which is parametrized via

$$A = 2rD\left(h + \frac{r}{2\cos(\Theta)}\left(2 - \sin(\Theta) - \frac{\arcsin(\cos(\Theta))}{\cos(\Theta)}\right)\right) \tag{A3}$$

and the depth D. Using the force balance $F_g = F_\sigma$, we obtain the rise height

$$h = \frac{\sigma\cos\Theta}{(\rho_2-\rho_1)gr} - \frac{r}{2\cos(\Theta)}\left(2-\sin(\Theta) - \frac{\arcsin(\cos(\Theta))}{\cos(\Theta)}\right). \tag{A4}$$

If the density contrast is high, the lower density can be neglected. This leads to the correlation

$$h = \frac{\sigma\cos\Theta}{\rho_2 gr} - \frac{r}{2\cos(\Theta)}\left(2 - \sin(\Theta) - \frac{\arcsin(\cos(\Theta))}{\cos(\Theta)}\right), \tag{A5}$$

which is typically found in the literature [77].

APPENDIX B: VOLUME CONSERVATION OF THE ALLEN-CAHN EQUATION

In this work, an Allen-Cahn approach is employed for the phase evolution. An Allen-Cahn approach without modifications is not volume preserving. If no additional evaporation velocity is considered, the surface terms lead to a volume change due to curvature minimization. However, the present approach leads to a volume-preserving Allen-Cahn equation, if the factor κ is set to zero. In this case, the term in

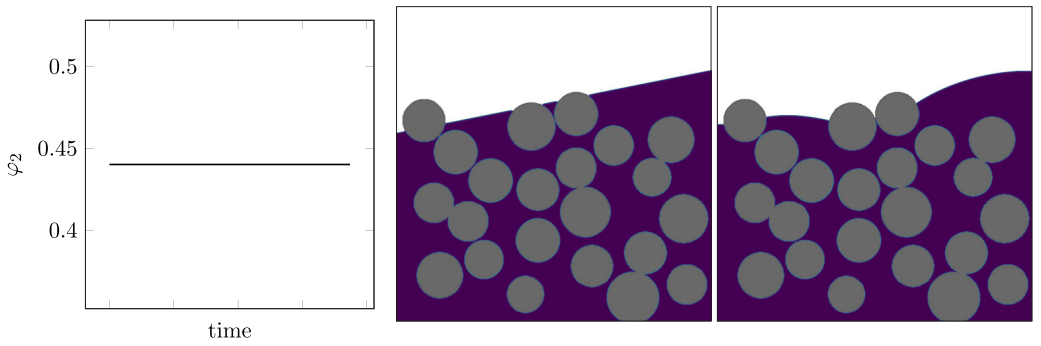

FIG. 13. Volume fraction of fluid φ_2 as a function of time (left), initial setting (middle), and final microstructure (right).

Eq. (10) gives an interfacial velocity that counteracts the volume shrinkage due to the curvature minimization dynamics. For $\kappa = 0$, the present model therefore corresponds to volume-preserving approaches, as in [49], using a Lagrange multiplier. Such an approach enforces the condition $\frac{d}{dt}\int \tilde{\varphi}\, \mathrm{d}t = 0$. It is to be noted that the curvature correction term [65] removes the curvature-minimizing dynamics and thus the corresponding volume change. However, in a numerical implementation this is only achieved approximately. Thus, a Lagrange multiplier is still required to ensure exact volume preservation. In this section, the expected behavior is to be validated. The initial values of the simulation can be found in Sec. III. Initially, three phases are set, with the solids colored gray and the fluids white and blue. In Fig. 13 on the left, the volume fraction of φ_2 (blue) is shown as a function of time for 480×480 cells. The middle and right images correspond to the initial and final states. The volume fraction is constant, while the surface changes according to the curvature minimization.

APPENDIX C: CONTACT ANGLE BEHAVIOR OF A STATIC CASE

Figure 14 sketches the development of the fluids for a point in time $t > t^0$. Due to the balance of forces between the surface tension and the volume force due to gravity, an angle $\Theta = \theta_1 + \theta_2 = 180^\circ - \theta$ is set at the three-phase interface in equilibrium with the help of the angles $\theta_2 = 90^\circ$ and θ_1, which is determined by the relationship

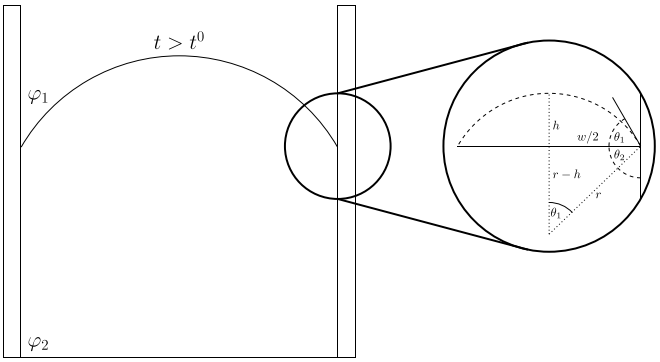

FIG. 14. Schematic drawing of the fluid distribution at any time $t > t^0$, with geometric relationships at the three-phase interface between the two fluids and the capillary wall.

$$\frac{2h}{w} = \tan\left(\frac{\theta_1}{2}\right). \tag{C1}$$

The parameters from Sec. III A are used for this simulation study, excluding κ, which is set to zero. Figure 15 shows the setting angle Θ as a function of time for different resolutions. The resolutions are 120×120, 240×240, and 480×480 for $n_x \times n_y$. All three resolutions follow the same behavior by starting with an initial angle of 90° and proceeding with an oscillation around the respective stationary solution before approaching it. With increasing refinement of the resolution, the deviation from the theoretical contact angle decreases. The values in equilibrium are $\Theta = 122.36$, $\Theta = 121.08$, and $\Theta = 119.81$, from the coarsest to the finest resolution. This simulation study reveals a converging behavior of the model capable to reproduce the wetting behavior for a stationary interface. The wetting behavior of a moving interface, taking evaporation into account, is found in Sec. III A.

APPENDIX D: DERIVATION OF THE DIFFUSE WETTING BOUNDARY CONDITION FOR THE ALLEN-CAHN APPROACH

To impose the moving boundary condition at the solid-fluid interface, we follow the approach of Li *et al.* [58]. The considered phase-field equation (8) is given by

$$\dot{\tilde{\varphi}} = M\left(\beta\partial_{\tilde{\varphi}}\psi - \alpha\left(\nabla^2\tilde{\varphi} - ||\nabla\tilde{\varphi}||\nabla\cdot\frac{\nabla\tilde{\varphi}}{||\nabla\tilde{\varphi}||}\right)\right) + v^{\mathrm{e}}||\nabla\tilde{\varphi}||, \quad \boldsymbol{x} \in V, \tag{D1}$$

with the boundary conditions (4):

$$\alpha\nabla\tilde{\varphi}\cdot\boldsymbol{n} = (\sigma_{2\mathrm{s}} - \sigma_{1\mathrm{s}})\partial_{\tilde{\varphi}}h^{\mathrm{ff}}(\tilde{\varphi}), \quad \boldsymbol{x} \in \partial V. \tag{D2}$$

First, we multiply the equation by the test function Ψ. Then we integrate over the fluid volume $V \subset \Omega$, with Ω as the whole domain. This gives the weak form of the equation and is represented by

$$0 = \int_V \Psi\dot{\tilde{\varphi}} - M\Psi\beta\partial_{\tilde{\varphi}}\psi + M\Psi\alpha\left(\nabla^2\tilde{\varphi} - ||\nabla\tilde{\varphi}||\nabla\cdot\frac{\nabla\tilde{\varphi}}{||\nabla\tilde{\varphi}||}\right) - \Psi v^{\mathrm{e}}||\nabla\tilde{\varphi}||\,\mathrm{d}V. \tag{D3}$$

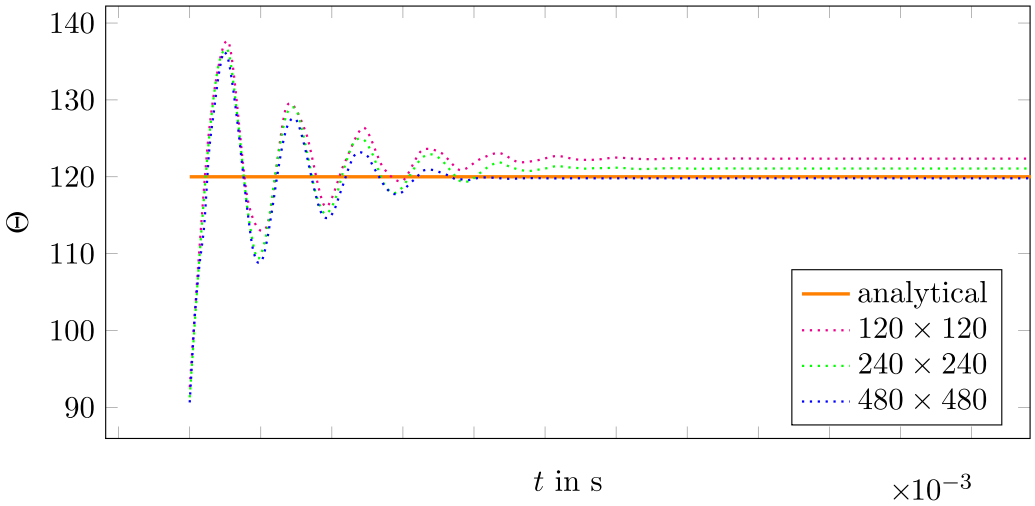

FIG. 15. Grid refinement for the static case with a contact angle of $\theta = 60^\circ$.

Taking into account the Gauss theorem, we obtain

$$0 = \int_V \Psi\dot{\tilde{\varphi}} - M\Psi\beta\partial_{\tilde{\varphi}}\psi - M\alpha\left(\nabla\tilde{\varphi}\cdot\nabla\Psi - ||\nabla\tilde{\varphi}||\nabla\cdot\frac{\nabla\tilde{\varphi}}{||\nabla\tilde{\varphi}||}\right) - \Psi v^{\mathrm{e}}||\nabla\tilde{\varphi}||\,\mathrm{d}V + \int_{\partial V}\alpha M\Psi\nabla\tilde{\varphi}\cdot\boldsymbol{n}\,\mathrm{d}S. \tag{D4}$$

Introducing the indicator function I and the Dirac distribution δ_Γ, Eq. (D4) can be written as an integral of the whole domain:

$$0 = \int_\Omega I\Psi\dot{\tilde{\varphi}} - M\Psi\beta I\partial_{\tilde{\varphi}}\psi - M\alpha I\left(\nabla\tilde{\varphi}\cdot\nabla\Psi - ||\nabla\tilde{\varphi}||\nabla\cdot\frac{\nabla\tilde{\varphi}}{||\nabla\tilde{\varphi}||}\right) - I\Psi v^{\mathrm{e}}||\nabla\tilde{\varphi}|| + M\delta_\Gamma\alpha\Psi\nabla\tilde{\varphi}\cdot\boldsymbol{n}\,\mathrm{d}V. \tag{D5}$$

Using the context

$$\int_\Omega \nabla\cdot(I\Psi\nabla\tilde{\varphi})\,\mathrm{d}V = \int_\Omega \Psi\nabla\cdot(I\nabla\tilde{\varphi})\,\mathrm{d}V + \int_\Omega I\nabla\tilde{\varphi}\cdot\nabla\Psi\,\mathrm{d}V, \tag{D6}$$

we receive

$$0 = \int_\Omega \Psi(I\dot{\tilde{\varphi}} + M\alpha\nabla\cdot(I\nabla\tilde{\varphi}) - M\alpha I\left(||\nabla\tilde{\varphi}||\nabla\cdot\frac{\nabla\tilde{\varphi}}{||\nabla\tilde{\varphi}||}\right) - M\beta I\partial_{\tilde{\varphi}}\psi - Iv^{\mathrm{e}}||\nabla\tilde{\varphi}|| + M\alpha\delta_\Gamma\nabla\tilde{\varphi}\cdot\boldsymbol{n})\,\mathrm{d}V. \tag{D7}$$

By applying the fundamental lemma of variation, we get, for $\boldsymbol{x}\in\Omega$,

$$I\dot{\tilde{\varphi}} = M\left(-\alpha\nabla\cdot(I\nabla\tilde{\varphi}) + M\alpha I\left(||\nabla\tilde{\varphi}||\nabla\cdot\frac{\nabla\tilde{\varphi}}{||\nabla\tilde{\varphi}||}\right) + \beta I\partial_{\tilde{\varphi}}\psi - \alpha\delta_\Gamma\nabla\tilde{\varphi}\cdot\boldsymbol{n}\right) + Iv^{\mathrm{e}}||\nabla\tilde{\varphi}||. \tag{D8}$$

Using the boundary condition in Eq. (4) to express the normal gradient $\nabla\tilde{\varphi}\cdot\boldsymbol{n}$, we obtain the following for $\boldsymbol{x}\in\Omega$:

$$I\dot{\tilde{\varphi}} = M\left(\beta I\partial_{\tilde{\varphi}}\psi + M\alpha I\left(||\nabla\tilde{\varphi}||\nabla\cdot\frac{\nabla\tilde{\varphi}}{||\nabla\tilde{\varphi}||}\right) - \alpha\nabla\cdot(I\nabla\tilde{\varphi}) - \delta_\Gamma(\sigma_{2\mathrm{s}}-\sigma_{1\mathrm{s}})\partial_{\tilde{\varphi}}h^{\mathrm{ff}}(\tilde{\varphi})\right) + Iv^{\mathrm{e}}||\nabla\tilde{\varphi}||. \tag{D9}$$

This sharp interface equation represents the boundary value problem, which consists of field equation (D1) and boundary conditions (D2). To transform the sharp interface model into the diffuse interface model, we approximate the indicator function by $I \approx h^{\mathrm{fs}}(\varphi^{\mathrm{f}})$ and the Dirac distribution as $\delta_\Gamma = ||\nabla I|| \approx \partial_{\varphi^{\mathrm{f}}}h^{\mathrm{fs}}(\varphi^{\mathrm{f}})||\nabla\varphi^{\mathrm{f}}||$. Thus, we finally get

$$\begin{aligned} h^{\mathrm{fs}}\dot{\tilde{\varphi}} = M\Bigg[&\beta h^{\mathrm{fs}}\partial_{\tilde{\varphi}}\psi - \alpha\left(\nabla\cdot(h^{\mathrm{fs}}\nabla\tilde{\varphi}) - h^{\mathrm{fs}}||\nabla\tilde{\varphi}||\nabla\cdot\frac{\nabla\tilde{\varphi}}{||\nabla\tilde{\varphi}||}\right) \\ &-\partial_{\varphi^{\mathrm{f}}}h^{\mathrm{fs}}(\varphi^{\mathrm{f}})||\nabla\varphi^{\mathrm{f}}||(\sigma_{2\mathrm{s}}-\sigma_{1\mathrm{s}})\partial_{\tilde{\varphi}}h^{\mathrm{ff}}(\tilde{\varphi})\Bigg] + h^{\mathrm{fs}}v^{\mathrm{e}}||\nabla\tilde{\varphi}||, \qquad \boldsymbol{x}\in\Omega. \end{aligned} \tag{D10}$$

APPENDIX E: DERIVATION OF THE THEORETICAL VOLUME FRACTION OF THE SOLVENT PHASE

According to Jaiser *et al.* [6], the drying rate during the constant rate period (CRP) can be calculated using the equation

$$\dot{r}_{\mathrm{solvent}} = \left.\frac{\mathrm{d}X}{\mathrm{d}t}\right|_{\mathrm{CRP}} M_{\mathrm{S}}. \tag{E1}$$

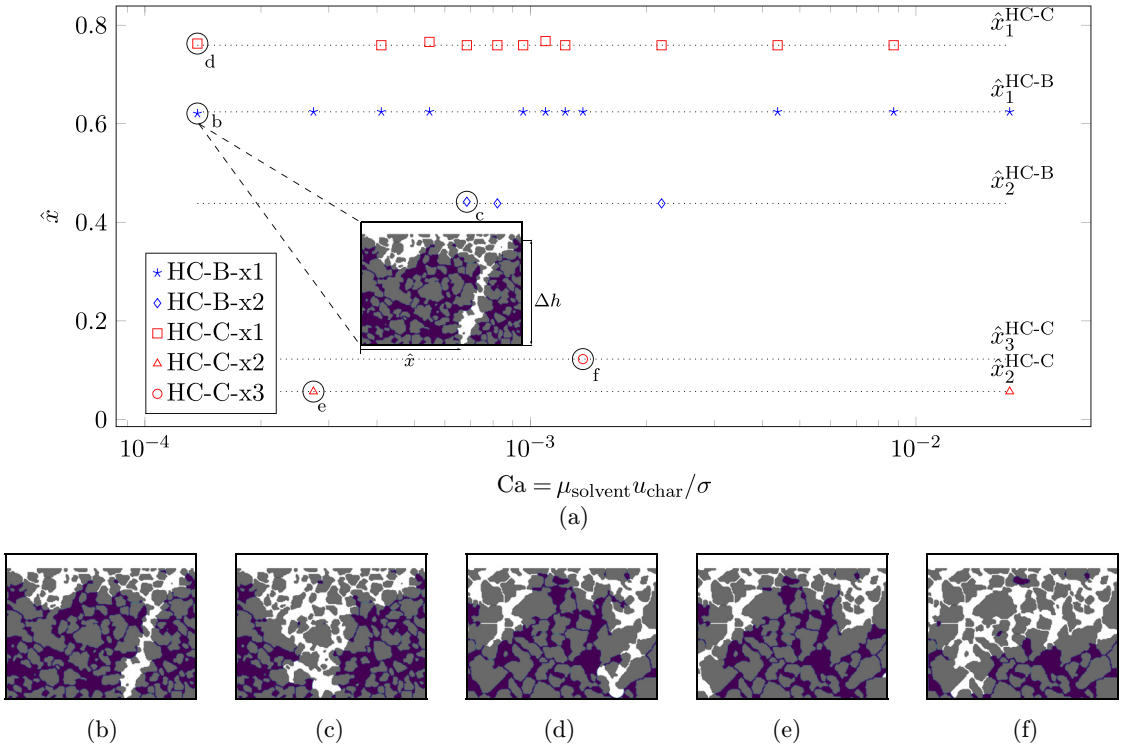

(a)

(b) (c) (d) (e) (f)

FIG. 16. (a) Dependence of the nondimensionalized $\hat{x}$ coordinate of the breakthrough point on the capillary number Ca for different microstructures. Data points relating to the HC-B and HC-B microstructure are represented by blue and red symbols. The horizontal lines represent the different clusters. Bottom: Simulation results for selected combinations of capillary numbers and $\hat{x}$ coordinates of the breakthrough point. The solvent is blue, the air is white, and particles are shown in gray. (b) HC-B-x1 ($\mathrm{Ca} = 1.368 \times 10^{-4}$), (c) HC-B-x2 ($\mathrm{Ca} = 6.84 \times 10^{-4}$), (d) HC-C-x1 ($\mathrm{Ca} = 1.368 \times 10^{-4}$), (e) HC-C-x2 ($\mathrm{Ca} = 2.736 \times 10^{-4}$), and (f) HC-C-x3 ($\mathrm{Ca} = 1.368 \times 10^{-3}$).

Here, $\dot{r}_{\mathrm{solvent}}$ is the area-specific evaporation rate in $\mathrm{kg\,m^{-2}\,s}$, X is the ratio of solvent to solid masses, with $X = \frac{m_{\mathrm{solvent}}}{m_{\mathrm{solid}}}$, t is the time in seconds, and M_{S} is the area-specific weight of the dry film in $\mathrm{kg\,m^{-2}}$. By integrating the equation and using the masses, we obtain

$$\frac{m_{\mathrm{solvent}}}{m_{\mathrm{solid}}} = \frac{m^0_{\mathrm{solvent}}}{m^0_{\mathrm{solid}}} - \frac{\dot{r}_{\mathrm{solvent}}}{M_{\mathrm{S}}} t. \tag{E2}$$

Here, the index 0 indicates the initial quantities. Equation (E2) can be expressed in terms of volume, using $V = m/\rho$, which results in the following for the volume of the solvent:

$$V_{\mathrm{solvent}} = V^0_{\mathrm{solvent}} - \frac{\rho_{\mathrm{solid}} V_{\mathrm{solid}}}{\rho_{\mathrm{solvent}} M_{\mathrm{S}}} \dot{r}_{\mathrm{solvent}} t. \tag{E3}$$

Introducing the variable $\chi_\alpha = \frac{V_\alpha}{V^0_{\mathrm{film}}}$ as the volume fraction of a phase α, related to the film volume $V^0_{\mathrm{film}} = V^0_{\mathrm{solvent}} + V_{\mathrm{solid}}$, we obtain

$$\chi_{\mathrm{solvent}} = -\frac{\rho_{\mathrm{solid}} \chi_{\mathrm{solid}}}{\rho_{\mathrm{solvent}} M_{\mathrm{S}}} \dot{r}_{\mathrm{solvent}} t + \chi^0_{\mathrm{solvent}}, \tag{E4}$$

by dividing Eq. (E3) by the volume. By introducing the abbreviation

$$\kappa = \frac{\rho_{\mathrm{solid}} \chi_{\mathrm{solid}}}{\rho_{\mathrm{solvent}} M_{\mathrm{S}}} \dot{r}_{\mathrm{solvent}}, \tag{E5}$$

we finally obtain the relationship

$$\chi_{\mathrm{solvent}} = -\kappa t + \chi^0_{\mathrm{solvent}}, \tag{E6}$$

with $\mathrm{s^{-1}}$ as unit for κ.

APPENDIX F: RESULTS FOR THE $\hat{x}$ COORDINATE

Figure 16(a) depicts the nondimensionalized $\hat{x}$ coordinate of the breakthrough point as a function of the capillary number for the microstructures HC-B and HC-C in blue and red, respectively. The $\hat{x}$ coordinates assume identical values for different capillary numbers. Figures 16(b)–16(f) illustrate the simulated microstructures at the time of breakthrough. Figures 16(b) and 16(c) refer to the HC-B microstructure, for the capillary numbers $\mathrm{Ca} = 1.368 \times 10^{-4}$ and $\mathrm{Ca} = 6.84 \times 10^{-4}$. A different $\hat{x}$ value can be observed for different capillary numbers. This is characterized by a differently favored capillary that forms until the breakthrough. The microstructure HC-C is given in the Figs. 16(d)–16(f) for the capillary numbers $\mathrm{Ca} = 1.368 \times 10^{-4}$, $\mathrm{Ca} = 2.736 \times 10^{-4}$, and $\mathrm{Ca} = 1.368 \times 10^{-3}$. All three capillary numbers supply different values for $\hat{x}$ and thus differently favored capillary pathways. Figures 16(d) and 16(e) differ slightly with respect to the height difference Δh. In summary, a significant influence of the microstructure and the viscosity, represented by a different capillary number, on the drying behavior can be observed.

[1] D. Larcher and J.-M. Tarascon, Towards greener and more sustainable batteries for electrical energy storage, Nat. Chem. **7**, 19 (2015).

[2] R. Usiskin, Y. Lu, J. Popovic, M. Law, P. Balaya, Y.-S. Hu, and J. Maier, Fundamentals, status and promise of sodium-based batteries, Nat. Rev. Mater. **6**, 1020 (2021).

[3] J. Klemens, A.-K. Wurba, D. Burger, M. Müller, W. Bauer, S. Büchele, O. Leonet, J. A. Blázquez, I. Boyano, E. Ayerbe *et al.*, Challenges and opportunities for large-scale electrode processing for sodium-ion and lithium-ion battery, Batteries Supercaps **6**, e202300291 (2023).

[4] M. Schütte, F. Degen, and H. Walter, Reducing energy consumption and greenhouse gas emissions of industrial drying processes in lithium-ion battery cell production: A qualitative technology benchmark, Batteries **10**, 64 (2024).

[5] B. Westphal, H. Bockholt, T. Günther, W. Haselrieder, and A. Kwade, Influence of convective drying parameters on electrode performance and physical electrode properties, ECS Trans. **64**, 57 (2015).

[6] S. Jaiser, M. Müller, M. Baunach, W. Bauer, P. Scharfer, and W. Schabel, Investigation of film solidification and binder migration during drying of Li-ion battery anodes, J. Power Sources **318**, 210 (2016).

[7] S. Jaiser, L. Funk, M. Baunach, P. Scharfer, and W. Schabel, Experimental investigation into battery electrode surfaces: The distribution of liquid at the surface and the emptying of pores during drying, J. Colloid Interface Sci. **494**, 22 (2017).

[8] S. Jaiser, J. Kumberg, J. Klaver, J. L. Urai, W. Schabel, J. Schmatz, and P. Scharfer, Microstructure formation of lithium-ion battery electrodes during drying—an ex-situ study using cryogenic broad ion beam slope-cutting and scanning electron microscopy (Cryo-BIB-SEM), J. Power Sources **345**, 97 (2017).

[9] B. G. Westphal and A. Kwade, Critical electrode properties and drying conditions causing component segregation in graphitic anodes for lithium-ion batteries, J. Energy Storage **18**, 509 (2018).

[10] J. Kumberg, M. Müller, R. Diehm, S. Spiegel, C. Wachsmann, W. Bauer, P. Scharfer, and W. Schabel, Drying of lithium-ion battery anodes for use in high-energy cells: Influence of electrode thickness on drying time, adhesion, and crack formation, Energy Technol. **7**, 1900722 (2019).

[11] J. Kumberg, M. Baunach, J. C. Eser, A. Altvater, P. Scharfer, and W. Schabel, Influence of layer thickness on the drying of lithium-ion battery electrodes—simulation and experimental validation, Energy Technol. **9**, 2100013 (2021).

[12] J. Kumberg, M. Baunach, J. C. Eser, A. Altvater, P. Scharfer, and W. Schabel, Investigation of drying curves of lithium-ion battery electrodes with a new gravimetrical double-side batch dryer concept including setup characterization and model simulations, Energy Technol. **9**, 2000889 (2021).

[13] J. Kumberg, W. Bauer, J. Schmatz, R. Diehm, M. Tönsmann, M. Müller, K. Ly, P. Scharfer, and W. Schabel, Reduced drying time of anodes for lithium-ion batteries through simultaneous multilayer coating, Energy Technol. **9**, 2100367 (2021).

[14] J. Klemens, L. Schneider, E. C. Herbst, N. Bohn, M. Müller, W. Bauer, P. Scharfer, and W. Schabel, Drying of NCM cathode electrodes with porous, nanostructured particles versus compact solid particles: Comparative study of binder migration as a function of drying conditions, Energy Technol. **10**, 2100985 (2022).

[15] J. Klemens, D. Burger, L. Schneider, S. Spiegel, M. Müller, N. Bohn, W. Bauer, H. Ehrenberg, P. Scharfer, and W. Schabel, Drying of compact and porous NCM cathode electrodes in different multilayer architectures: Influence of layer configuration and drying rate on electrode properties, Energy Technol. **11**, 2300267 (2023).

[16] J. Klemens, L. Schneider, D. Burger, N. Zimmerer, M. Müller, W. Bauer, H. Ehrenberg, P. Scharfer, and W. Schabel, Process and drying behavior toward higher drying rates of hard carbon anodes for sodium-ion batteries with different particle sizes: An experimental study in comparison to graphite for lithium-ion-batteries, Energy Technol. **11**, 2300338 (2023).

[17] F. Font, B. Protas, G. Richardson, and J. M. Foster, Binder migration during drying of lithium-ion battery electrodes: Modelling and comparison to experiment, J. Power Sources **393**, 177 (2018).

[18] C. Zihrul, S. Wolf, and A. Kwade, Model experiments for explaining the processes occurring during conductive battery electrode drying, Energy Technol. **11**, 2200671 (2023).

[19] M. M. Forouzan, C.-W. Chao, D. Bustamante, B. A. Mazzeo, and D. R. Wheeler, Experiment and simulation of the fabrication process of lithium-ion battery cathodes for determining microstructure and mechanical properties, J. Power Sources **312**, 172 (2016).

[20] C. Liu, T. Lombardo, J. Xu, A. C. Ngandjong, and A. A. Franco, An experimentally-validated 3D electrochemical model revealing electrode manufacturing parameters' effects on battery performance, Energy Storage Mater. **54**, 156 (2023).

[21] M. Lippke, T. Ohnimus, T. Heckmann, D. Ivanov, P. Scharfer, W. Schabel, C. Schilde, and A. Kwade, Simulation of structure formation during drying of lithium-ion battery electrodes using discrete element method, Energy Technol. **11**, 2200724 (2023).

[22] S. Wolf, M. Lippke, A. Schoo, A. Kwade, and C. Schilde, A computational fluid dynamics–discrete element method model for physics-based simulation of structure formation during battery electrode drying, Energy Technol. **12**, 2301004 (2024).

[23] X. Ye, Z. Yang, X. Liu, Q. Lu, S. Yuan, and F. Jiang, Optimizing porous medium electrode suspension drying: A numerical simulation, Phys. Fluids **36**, 075186 (2024).

[24] N. Susarla, S. Ahmed, and D. W. Dees, Modeling and analysis of solvent removal during Li-ion battery electrode drying, J. Power Sources **378**, 660 (2018).

[25] M. Stein, A. Mistry, and P. P. Mukherjee, Mechanistic understanding of the role of evaporation in electrode processing, J. Electrochem. Soc. **164**, A1616 (2017).

[26] A. C. Ngandjong, A. Rucci, M. Maiza, G. Shukla, J. Vazquez-Arenas, and A. A. Franco, Multiscale simulation platform linking lithium ion battery electrode fabrication process with performance at the cell level, J. Phys. Chem. Lett. **8**, 5966 (2017).

[27] A. Rucci, A. C. Ngandjong, E. N. Primo, M. Maiza, and A. A. Franco, Tracking variabilities in the simulation of lithium ion battery electrode fabrication and its impact on electrochemical performance, Electrochim. Acta **312**, 168 (2019).

[28] M. Chouchane, A. Rucci, T. Lombardo, A. C. Ngandjong, and A. A. Franco, Lithium ion battery electrodes predicted from manufacturing simulations: Assessing the impact of the

carbon-binder spatial location on the electrochemical performance, J. Power Sources **444**, 227285 (2019).

[29] T. Lombardo, J.-B. Hoock, E. N. Primo, A. C. Ngandjong, M. Duquesnoy, and A. A. Franco, Accelerated optimization methods for force-field parametrization in battery electrode manufacturing modeling, Batteries Supercaps **3**, 721 (2020).

[30] T. Lombardo, A. C. Ngandjong, A. Belhcen, and A. A. Franco, Carbon-binder migration: A three-dimensional drying model for lithium-ion battery electrodes, Energy Storage Mater. **43**, 337 (2021).

[31] A. Shodiev, E. N. Primo, M. Chouchane, T. Lombardo, A. C. Ngandjong, A. Rucci, and A. A. Franco, 4D-resolved physical model for electrochemical impedance spectroscopy of $Li(Ni_{1-x-y}Mn_xCo_y)O_2$-based cathodes in symmetric cells: Consequences in tortuosity calculations, J. Power Sources **454**, 227871 (2020).

[32] C. Liu, O. Arcelus, T. Lombardo, H. Oularbi, and A. A. Franco, Towards a 3D-resolved model of Si/graphite composite electrodes from manufacturing simulations, J. Power Sources **512**, 230486 (2021).

[33] A. C. Ngandjong, T. Lombardo, E. N. Primo, M. Chouchane, A. Shodiev, O. Arcelus, and A. A. Franco, Investigating electrode calendering and its impact on electrochemical performance by means of a new discrete element method model: Towards a digital twin of Li-ion battery manufacturing, J. Power Sources **485**, 229320 (2021).

[34] T. Lombardo, F. Lambert, R. Russo, F. M. Zanotto, C. Frayret, G. Toussaint, P. Stevens, M. Becuwe, and A. A. Franco, Experimentally validated three-dimensional modeling of organic-based sodium-ion battery electrode manufacturing, Batteries Supercaps **5**, e202200116 (2022).

[35] J. Xu, A. C. Ngandjong, C. Liu, F. M. Zanotto, O. Arcelus, A. Demortiere, and A. A. Franco, Lithium ion battery electrode manufacturing model accounting for 3D realistic shapes of active material particles, J. Power Sources **554**, 232294 (2023).

[36] M. Lippke, T. Ohnimus, F. Frankenberg, C. Schilde, and A. Kwade, Drying and calendering of lithium ion battery electrodes: A combined simulation approach, Powder Technol. **444**, 119984 (2024).

[37] C. W. Hirt and B. D. Nichols, Volume of fluid (VOF) method for the dynamics of free boundaries, J. Comput. Phys. **39**, 201 (1981).

[38] X. Lu, From microscale to macroscale modeling of drying porous media, Ph.D. thesis, Otto von Guericke University of Magdeburg, 2021, http://dx.doi.org/10.25673/77035.

[39] S. Whitaker, Simultaneous heat, mass, and momentum transfer in porous media: A theory of drying, in *Advances in Heat Transfer*, Vol. 13 (Elsevier, Amsterdam, 1977), pp. 119–203.

[40] M. Prat, Percolation model of drying under isothermal conditions in porous media, Int. J. Multiphase Flow **19**, 691 (1993).

[41] T. Metzger and E. Tsotsas, Influence of pore size distribution on drying kinetics: A simple capillary model, Drying Technol. **23**, 1797 (2005).

[42] T. Metzger, A. Irawan, and E. Tsotsas, Influence of pore structure on drying kinetics: A pore network study, AIChE J. **53**, 3029 (2007).

[43] T. Metzger, A. Irawan, and E. Tsotsas, Isothermal drying of pore networks: Influence of friction for different pore structures, Drying Technol. **25**, 49 (2007).

[44] T. Metzger and E. Tsotsas, Viscous stabilization of drying front: Three-dimensional pore network simulations, Chem. Eng. Res. Des. **86**, 739 (2008).

[45] S. T. Pham, B. Chareyre, E. Tsotsas, and A. Kharaghani, Pore network modeling of phase distribution and capillary force evolution during slow drying of particle aggregates, Powder Technol. **407**, 117627 (2022).

[46] O. Chapuis and M. Prat, Influence of wettability conditions on slow evaporation in two-dimensional porous media, Phys. Rev. E **75**, 046311 (2007).

[47] H. Chraibi, M. Prat, and O. Chapuis, Influence of contact angle on slow evaporation in two-dimensional porous media, Phys. Rev. E **79**, 026313 (2009).

[48] I. Steinbach and F. Pezzolla, A generalized field method for multiphase transformations using interface fields, Physica D **134**, 385 (1999).

[49] B. Nestler, H. Garcke, and B. Stinner, Multicomponent alloy solidification: Phase-field modeling and simulations, Phys. Rev. E **71**, 041609 (2005).

[50] M. Reder, J. Holland-Cunz, P. Lorson, A. August, and B. Nestler, Simulative determination of effective mechanical properties for digitally generated foam geometries, Adv. Eng. Mater. **25**, 2300340 (2023).

[51] D. Qu and H.-C. Yu, Multiphysics electrochemical impedance simulations of complex multiphase graphite electrodes, ACS Appl. Energy Mater. **6**, 3468 (2023).

[52] T. Takaki, R. Sato, R. Rojas, M. Ohno, and Y. Shibuta, Phase-field lattice Boltzmann simulations of multiple dendrite growth with motion, collision, and coalescence and subsequent grain growth, Comput. Mater. Sci. **147**, 124 (2018).

[53] M. Reder, D. Schneider, F. Wang, S. Daubner, and B. Nestler, Phase-field formulation of a fictitious domain method for particulate flows interacting with complex and evolving geometries, Int. J. Numer. Methods Fluids **93**, 2486 (2021).

[54] M. Reder, P. W. Hoffrogge, D. Schneider, and B. Nestler, A phase-field based model for coupling two-phase flow with the motion of immersed rigid bodies, Int. J. Numer. Methods Eng. **123**, 3757 (2022).

[55] S. Daubner, M. Weichel, D. Schneider, and B. Nestler, Modeling intercalation in cathode materials with phase-field methods: Assumptions and implications using the example of $LiFePO_4$, Electrochim. Acta **421**, 140516 (2022).

[56] S. Daubner, M. Dillenz, L. F. Pfeiffer, C. Gauckler, M. Rosin, N. Burgard, J. Martin, P. Axmann, M. Sotoudeh, A. Groß *et al.*, Combined study of phase transitions in the P2-type $Na_xNi_{1/3}Mn_{2/3}O_2$ cathode material: Experimental, ab-initio and multiphase-field results, npj Comput. Mater. **10**, 75 (2024).

[57] P. C. Hohenberg and B. I. Halperin, Theory of dynamic critical phenomena, Rev. Mod. Phys. **49**, 435 (1977).

[58] X. Li and A. Rätz, Solving PDEs in complex geometries: A diffuse domain approach, Commun. Math. Sci. **7**, 81 (2009).

[59] M. Ruzicka, Analysis of generalized Newtonian fluids, Top. Math. Fluid Mech. **2073**, 199 (2013).

[60] M. Reder, A. Prahs, D. Schneider, and B. Nestler, Viscous stress approximations in diffuse interface methods for two-phase flow based on mechanical jump conditions, Comput. Methods Appl. Mech. Eng. **432**, 117341 (2024).

[61] C. G. Gal and T. T. Medjo, On a regularized family of models for homogeneous incompressible two-phase flows, J. Nonlinear Sci. **24**, 1033 (2014).

[62] D. Jacqmin, Calculation of two-phase Navier–Stokes flows using phase-field modeling, J. Comput. Phys. **155**, 96 (1999).

[63] D. Jacqmin, An energy approach to the continuum surface tension method, in *34th Aerospace Sciences Meeting and Exhibit* (AIAA, Reston, VA, 1996), p. 858.

[64] E. Schoof, D. Schneider, N. Streichhan, T. Mittnacht, M. Selzer, and B. Nestler, Multiphase-field modeling of martensitic phase transformation in a dual-phase microstructure, Int. J. Solids Struct. **134**, 181 (2018).

[65] Y. Sun and C. Beckermann, Sharp interface tracking using the phase-field equation, J. Comput. Phys. **220**, 626 (2007).

[66] C. Beckermann, H.-J. Diepers, I. Steinbach, A. Karma, and X. Tong, Modeling melt convection in phase-field simulations of solidification, J. Comput. Phys. **154**, 468 (1999).

[67] S. Aland, J. Lowengrub, and A. Voigt, Two-phase flow in complex geometries: A diffuse domain approach, Comput. Model. Eng. Sci. **57**, 77 (2010).

[68] J. Hötzer, A. Reiter, H. Hierl, P. Steinmetz, M. Selzer, and B. Nestler, The parallel multi-physics phase-field framework pace3d, J. Comput. Sci. **26**, 1 (2018).

[69] N. P. Waterson and H. Deconinck, Design principles for bounded higher-order convection schemes—a unified approach, J. Comput. Phys. **224**, 182 (2007).

[70] K. O. Friedrichs, Symmetric hyperbolic linear differential equations, Commun. Pure Appl. Math. **7**, 345 (1954).

[71] A. Kharaghani, Drying and wetting of capillary porous materials: Insights from imaging and physics-based modeling, Ph.D. thesis, Habilitationsschrift, Magdeburg, Otto-von-Guericke-Universität Magdeburg (2020).

[72] O. Krischer and K. Kröll, *Die Wissenschaftlichen Grundlagen der Trocknungstechnik* (Springer-Verlag, Berlin, 2013).

[73] L. Griem, P. Zschumme, M. Laqua, N. Brandt, E. Schoof, P. Altschuh, and M. Selzer, Kadistudio: Fair modelling of scientific research processes, Data Sci. J. **21**, 16 (2022).

[74] A. Benchabane and K. Bekkour, Rheological properties of carboxymethyl cellulose (CMC) solutions, Colloid Polym. Sci. **286**, 1173 (2008).

[75] H. Abels, H. Garcke, and G. Grün, Thermodynamically consistent, frame indifferent diffuse interface models for incompressible two-phase flows with different densities, Math. Models Methods Appl. Sci. **22**, 1150013 (2012).

[76] M. Weichel, Raw data for plots, Zenodo (2025), https://doi.org/10.5281/zenodo.14931206.

[77] D. Gründing, M. Smuda, T. Antritter, M. Fricke, D. Rettenmaier, F. Kummer, P. Stephan, H. Marschall, and D. Bothe, A comparative study of transient capillary rise using direct numerical simulations, Appl. Math. Modell. **86**, 142 (2020).